



## Cloud property estimates from zenith spectral measurements of scattered sunlight between 0.9 and 1.7 $\mu\text{m}$

J. S. Daniel,<sup>1</sup> R. W. Portmann,<sup>1</sup> H. L. Miller,<sup>1,2</sup> S. Solomon,<sup>1</sup> A. O. Langford,<sup>1</sup>  
C. S. Eubank,<sup>1,2</sup> R. Schofield,<sup>1,2</sup> D. D. Turner,<sup>3,4</sup> and M. D. Shupe<sup>5,6</sup>

Received 2 September 2005; revised 20 December 2005; accepted 12 April 2006; published 29 August 2006.

[1] A theoretical approach is used to quantify the information available to retrieve cloud physical properties from data taken by a ground-based spectrometer measuring scattered sunlight in the near-infrared wavelength region. Three wavelength regions between 0.9 and 1.7  $\mu\text{m}$ , each containing water vapor, liquid, and ice absorption features, are examined using a differential optical absorption spectroscopy optimal estimation retrieval technique. Cloud properties that can be retrieved include path-integrated liquid water path and path-integrated ice water path (PLWP and PIWP), cloud liquid and ice temperatures, and the second moment of the photon path distribution. The accuracy of these cloud property retrievals is estimated for a variety of simulated conditions, with key analysis assumptions identified. The sensitivity of the measurements in the longest wavelength region to liquid water and ice is high, allowing for accurate estimates of PLWP and PIWP under optically thin clouds, while the shorter two wavelength bands provide more information under optically thicker clouds. Observations of mixed-phase clouds over Barrow, Alaska, are used to illustrate the practicality of the technique. Retrieved LWP values (inferred from PLWP) are compared to LWP estimates from a microwave radiometer and an atmospheric emitted radiance interferometer; PIWP estimates are compared to IWP estimates from a millimeter-wave cloud radar. Cloud liquid temperature and photon path distribution information retrieved from these data are also presented. Furthermore, we suggest a technique for combining near-infrared spectral PLWP measurements with microwave radiometer observations to estimate cloud droplet effective radius.

**Citation:** Daniel, J. S., R. W. Portmann, H. L. Miller, S. Solomon, A. O. Langford, C. S. Eubank, R. Schofield, D. D. Turner, and M. D. Shupe (2006), Cloud property estimates from zenith spectral measurements of scattered sunlight between 0.9 and 1.7  $\mu\text{m}$ , *J. Geophys. Res.*, 111, D16208, doi:10.1029/2005JD006641.

### 1. Introduction

[2] The importance of clouds to the accurate modeling of our climate system has been recognized for over two decades [Ramanathan *et al.*, 1983]. Differences in the proper manner to represent clouds and cloud processes in general circulation models (GCMs) remain a significant source of the variation in estimates of the future climate impact of greenhouse gases [Intergovernmental Panel on Climate Change (IPCC), 2001]. The response of clouds to the presence of aerosols is also increasingly being examined as a potentially important term in future climate forcing with

even the sign of the forcing unknown [Lohmann and Feichter, 2005]. Most of the unresolved cloud questions such as these are complicated and likely will not be solved without more complete atmospheric observations than are currently available.

[3] Numerous methods have been used to measure cloud properties. In situ measurements of quantities such as drop size distribution and liquid water content (LWC) can be quite beneficial for process studies [Johnson *et al.*, 2000, and references therein], but such measurements are expensive to make and are generally limited both spatially and temporally, making it difficult to develop a global understanding. Ground- and/or satellite-based observations likely represent the best method to acquire cloud information over large geographic scales, but interpretation of these observations can be difficult. Some of the earliest analyses of passive remote cloud observations relied on using reflected near-infrared solar radiation to infer both cloud optical depth and thermodynamic phase, as well as cloud droplet effective radius [Hansen and Pollack, 1970; Sagan and Pollack, 1967]. As Earth-observing satellites became more numerous and measurement quality improved, these retrieval methods advanced as well [Arking and Childs, 1985; Nakajima and King, 1990; Pilewskie and Twomey, 1987;

<sup>1</sup>Aeronomy Laboratory, NOAA, Boulder, Colorado, USA.

<sup>2</sup>Also at Cooperative Institute for Research in Environmental Sciences, University of Colorado, Boulder, Colorado, USA.

<sup>3</sup>Pacific Northwest National Laboratory, Richland, Washington, USA.

<sup>4</sup>Now at Space Science and Engineering Center, University of Wisconsin, Madison, USA.

<sup>5</sup>Cooperative Institute for Research in Environmental Sciences, University of Colorado, Boulder, Colorado, USA.

<sup>6</sup>Also at Environmental Technology Laboratory, NOAA, Boulder, Colorado, USA.

Twomey and Cocks, 1989]. It was recognized that information found at terrestrial infrared wavelengths could also provide information concerning liquid water path (LWP) and liquid optical depth [Han et al., 1995; Kawamoto et al., 2001; Nakajima and Nakajima, 1995; Turner, 2005], and ice water path (IWP) and ice optical depth [Ackerman et al., 1995; Liu and Illingworth, 2000; Minnis et al., 1993; Ou et al., 1993]. Infrared wavelengths also provide information about cloud top temperatures [Arking and Childs, 1985; Liou et al., 1990; Minnis et al., 1993; Ou et al., 1993; Szejwach, 1982] as well as thermodynamic phase [Ackerman et al., 1990; Baum et al., 2000; Strabala et al., 1994; Turner et al., 2003].

[4] If total column LWP or IWP is desired, for input into climate or weather models, for example, perhaps the most direct method is to passively measure the emission of cloud microwave radiation [Crewell and Lohnert, 2003; Deeter and Evans, 2000; Liu and Curry, 1998; Lohnert and Crewell, 2003; Westwater, 1978; Zhao and Weng, 2002]. Radiation at these wavelengths can also provide information about cloud liquid temperature, although with large uncertainties for optically thin clouds [Lin et al., 1998]; a similar limitation applies to infrared data. Recently, it has been suggested that higher microwave frequencies (submillimeter wavelengths) have benefits for probing ice clouds more fully [Evans et al., 1999, 1998]. Some of the same information acquired with passive microwave observations can be obtained actively using radar, with the additional benefit of acquiring profile information [e.g., Frisch et al., 1995; Matrosov et al., 1994, 1992; Shupe et al., 2001]. However, a significant difficulty in interpreting radar observations is the scattering dependence on the sixth moment of the particle size distribution. This makes it challenging to infer quantitatively accurate information about the third moment of the distribution (approximate volume). Lidar is yet another active measurement technique that has a long history [Hinkley, 1976; Wilczak et al., 1996, and references therein] and can be very useful in probing thin clouds [e.g., Platt, 1973].

[5] In this work, our primary focus is on the retrieval of path-integrated liquid water path (PLWP), path-integrated ice water path (PIWP), cloud liquid and ice temperatures, and photon path distribution information. We also propose a technique that demonstrates the potential benefits of using ground-based, near-infrared, zenith-sky spectral observations in a complementary fashion with other observations. Specifically, we suggest a method of combining the near-infrared PLWP retrieval with the dual-channel microwave radiometer LWP values to yield cloud droplet effective radius estimates. Indeed, the benefits of combining multiple instruments is recognized and used in many of the previously referenced studies. Even the combination of ground- and satellite-based observations are shown to be highly beneficial at times [Miller et al., 2000].

[6] PLWP and PIWP differ from LWP and IWP in that LWP and IWP represent the amount of liquid and ice vertically across the cloud, while the path-integrated quantities represent the amount of liquid and ice encountered by the photons as they scatter through the cloud [Daniel et al., 2002]. Both LWP and IWP are critically important to the calculation of the atmospheric radiative balance as these are the values prescribed in models performing radiative trans-

fer calculations. The path-integrated quantities do not have unique relationships to LWP and IWP, but depend on numerous cloud parameters (e.g., cloud size distribution, photon path distribution, three-dimensional effects, etc.). Nevertheless, acceptable relationships can be calculated in many circumstances by making reasonable microphysical and macrophysical cloud assumptions. PLWP and PIWP quantities estimated from ground-based observations follow directly from the measured fractional absorption of the transmitted beam due to the various water phases. This fractional absorption can also be used to validate weather and climate models, while simultaneous downlooking measurements above the cloud could even allow for absolute estimates of cloud absorption by each of the water phases.

[7] Cloud temperature is a radiatively important quantity as well as LWP and IWP. The cloud top temperature is important in determining the amount of outgoing longwave radiation (OLR) and therefore can affect the amount of surface cloud radiative forcing [Shupe and Intrieri, 2004]. The relationship of LWP with cloud temperature is important and could have implications for the response of clouds to a changing temperature environment and thus for the cloud feedback to greenhouse forcing. Recent studies suggest that this LWP response is dependent on the type and location of the cloud, with LWP increasing with increasing T in the Arctic [Lin et al., 2003] and decreasing with increasing T in the warm months at the Department of Energy's (DOE) Atmospheric Radiation Measurement (ARM) Southern Great Plains (SGP) site [Del Genio and Wolf, 2000]. In both cases, the cause of the LWP change was the change in cloud thickness, and not the changing LWC as has been suggested by some earlier modeling studies [Betts and Harshvardhan, 1987; Somerville and Remer, 1984]. It also has been suggested that ice particle size distributions are dependent on cloud temperature [Heymsfield et al., 2000] and that relationships can be derived among IWC, effective size, and temperature [Sun and Rikus, 1999]. Finally, the detection of supercooled water has obvious implications for detecting icing conditions and aircraft safety. The measurements of liquid and ice temperature for optically thinner clouds are of particular interest, as the clouds' lower optical depths make temperature and LWP/IWP retrievals, and even cloud detection, from satellite more problematic. For optically thicker clouds, the temperature retrieved from transmitted light is more closely related to the mean cloud temperature than the cloud top temperature retrieved by infrared satellite techniques or downlooking near-infrared observations [see, e.g., Platnick, 2000].

[8] Statistics concerning the photon path distribution can be useful in comparing cloud radiative transfer calculations with observations. Ideally, the second moment of the path distribution can be used to identify 3-D cloud effects [Marshak et al., 1995]. Path distribution information can also be critical to estimating LWP and IWP when the absorption features are not optically thin. This problem could be particularly great in cases when spectral measurements are not available and only radiances (or irradiances) at a few discrete wavelengths are measured. Estimates of the second moment of the path distribution from observations have typically used the oxygen A-band [Min and

*Clothiaux*, 2003; *Min and Harrison*, 1999; *Min et al.*, 2001; *Pfeilsticker et al.*, 1998; *Veitel et al.*, 1998] with the recent addition of the water vapor band at 0.82  $\mu\text{m}$  [*Min et al.*, 2004]. We take a different approach by deriving photon statistics where liquid water is a significant absorber; this is a fundamentally different measure, as discussed in section 3, than if calculated from  $\text{O}_2$  or water vapor absorption.

[9] The technique on which this work is based uses measurements of scattered solar radiation in the near-infrared and represents an improvement to the technique described by *Daniel et al.* [2002]. In that study the vapor, liquid, and ice absorption bands between about 0.86 and 1.06  $\mu\text{m}$  were used to estimate the PLWP and PIWP quantities for a range of larger cloud optical depths; it was hypothesized in that study and confirmed here that consideration of the stronger absorption bands at longer wavelengths could increase the sensitivity of the technique. Significant strengths of this retrieval method are that it considers only spectral shape rather than low-frequency spectral changes (due to, e.g., Rayleigh and aerosol scattering and aerosol absorption), it does not require a complicated radiative transfer model with its implicit atmospheric assumptions, and it does not rely on absolute calibration or even require specific knowledge of the detailed low-frequency instrumental spectral response.

[10] In this work, we quantify our ability to estimate the aforementioned cloud quantities using the three water bands between 0.9 and 1.6  $\mu\text{m}$ . It should be noted that the use of the shorter wavelength bands (0.9–1.3  $\mu\text{m}$ ) are rarely discussed, although they provide more cloud information under optically thicker clouds than can the longer, more saturated wavelengths. PLWP quantities are estimated from data taken at the ARM site in Barrow, Alaska, and using a radiative transfer model are compared to LWP estimates from microwave radiometer (MWR) and atmospheric emitted radiance interferometer (AERI) data; PIWP estimates are compared to IWP estimates from millimeter-wavelength cloud radar (MMCR) data. Cloud liquid temperature and the photon path distribution width are also retrieved and evaluated in terms of their likely accuracy.

[11] The forward modeling and retrieval technique are discussed in section 2. Theoretical calculations used to quantify the information available to estimate the cloud properties from these wavelengths are presented in section 3, with the experimental observations and comparisons found in section 4. Conclusions are presented in section 5.

## 2. Method

[12] In the retrieval process, known absorption spectral features are fit to the ratio of a foreground to a background spectrum. Hence the spectral information arises partly from differences in the atmospheric state at the times when the foreground and background spectra were measured. The primary advantage of using the ratio of spectra is that many variations with wavelength due to, for example, instrumental response and solar structure, cancel out and do not adversely affect the retrievals. Also, the detrimental effects of interfering gases, such as water vapor, that can limit the accuracy of cloud retrievals are reduced; this will be shown in more detail in sections 3 and 4.

[13] Theoretical evaluation of the retrieval technique is performed by calculating synthetic spectra using a discrete-ordinate, plane-parallel radiative transfer model (DISORT2.0 [*Stamnes et al.*, 1988]) and retrieving the cloud parameters from these spectra using an optimal estimation [*Rodgers*, 2000] differential optical absorption spectroscopy (DOAS) method. Downwelling spectral radiances at the surface are calculated every 0.1  $\text{cm}^{-1}$  from 0.87 to 1.65  $\mu\text{m}$  (11,490 to 6060  $\text{cm}^{-1}$ ) with the multiple scattering model, considering Rayleigh scattering, cloud (liquid and ice) absorption and scattering, and absorption due to water vapor, carbon dioxide, oxygen, the oxygen collision complex ( $\text{O}_4$ ), and methane. These radiances are convolved with a 6 nm full-width-half-maximum (FWHM) Gaussian function to simulate the slit function of a moderately resolving instrument. The model is run with 15 vertical layers, each with a thickness of 1 km, and with eight streams, where the most downwelling stream is taken to be representative of the observed intensity by the zenith-viewing instrument. The calculations are performed with a constant surface albedo of 0.2.

[14] Gaseous absorption coefficients are calculated as in the work of *Daniel et al.* [1999] using the HITRAN 2000 spectral database [*Rothman et al.*, 1998]. Liquid water extinction,  $\omega$  (single scattering albedo), and  $g$  (asymmetry factor) values are calculated at 265 K and 295 K from Mie theory [*Wiscombe*, 1979] using imaginary refractive indices from *Kou et al.* [1993] and real refractive indices from *Segelstein* [1981]. The cloud liquid size distribution over which the Mie calculations are integrated is assumed to be lognormal of the form

$$n(r)dr = Ar^\gamma \exp(-Br) \quad (1)$$

[*Jursa*, 1985]. Linear interpolation is used to estimate the scattering parameters at temperatures between these two limits. The liquid water asymmetry factors are included in the forward model using the *Henyey and Greenstein* [1941] approximation. Ice scattering parameterizations are based on the calculations of *Yang et al.* [2000] for the smooth aggregate habit. In order to include the effect of the ice absorption temperature dependence we have altered the *Yang et al.* [2000] single scattering values to be consistent with the imaginary refractive index measurements of *Grundy and Schmitt* [1998] at 10 K increments between 210 K and 270 K. As with the liquid, linear interpolation is used between these 10 K increments. Because of the potentially large forward scattering term for ice particles, rather than using the Henyey-Greenstein approximation, 512 Legendre moments are calculated every 100 nm (with the values linearly interpolated in between) and used in the multiple scattering model, which takes advantage of the *Nakajima and Tanaka* [1988] approximation to better approximate the sharp forward scattering lobe when using a relatively small number of discrete-ordinate streams.

[15] Retrieved quantities include PLWP, PIWP, path-integrated water vapor,  $\text{O}_2$ ,  $\text{CO}_2$ ,  $\text{O}_4$ ,  $\text{CH}_4$ , a constant, and terms varying linearly and quadratically with wavelength. Also included are liquid and ice temperature, a path distribution width parameter ( $\alpha$ ), and the fraction of water vapor affected by the path enhancement. The retrieval model fits the cross sections of known absorbers to the ratio of a

foreground to a background spectrum described by the equation

$$\frac{I_f}{I_b} = (a + b\lambda + c\lambda^2) \frac{S_f \otimes \int_{-\infty}^{\infty} K(\lambda') F(\lambda - \lambda') d\lambda'}{S_b \otimes \int_{-\infty}^{\infty} K(\lambda') B(\lambda - \lambda') d\lambda'}, \quad (2)$$

where  $\lambda$  is the wavelength in microns,  $a$ ,  $b$ , and  $c$  are constants, and  $I$  is the measured spectral radiance. All  $f$  and  $b$  subscripts refer to quantities representative of the foreground and background spectra, respectively, with the foreground quantities retrieved and the background quantities prescribed.  $S$  represents the shift and stretch operations used when analyzing measurements, which allow for the displacement of the wavelength/pixel relationship of the measured spectrum relative to the calibrated relationship to assure the measurements are spectrally aligned with the absorption cross sections. The function  $K$  represents the instrument slit function. The functions  $F$  and  $B$  are the modeled foreground and background spectra, given by

$$B(\lambda) = \exp \left\{ -(1 - P_b) \left( \sum_{gases} \sigma_i n_i \right) \right\} \times \alpha_b^{\alpha_b} \cdot \left[ \alpha_b + e_L \frac{\gamma_L}{\rho_L} LWP_b + e_I \frac{\gamma_I}{\rho_I} IWP_b + P_b \left( \sum_{gases} \sigma_i n_i \right) \right]^{-\alpha_b} \quad (3)$$

$$F(\lambda) = \exp \left\{ -(1 - P_f) \left( \sum_{gases} \sigma_i n_i \right) \right\} \times \alpha_f^{\alpha_f} \cdot \left[ \alpha_f + e_L \frac{\gamma_L}{\rho_L} LWP_f + e_I \frac{\gamma_I}{\rho_I} IWP_f + P_f \left( \sum_{gases} \sigma_i n_i \right) \right]^{-\alpha_f} \quad (4)$$

where  $e$  is the cloud path enhancement for liquid or ice,  $\gamma$  is the calculated volume absorption coefficient for particles of a particular size,  $\rho$  is the density, and the subscripts  $L$  and  $I$  refer to quantities pertaining to liquid and ice, respectively. The terms  $\sigma_i$  are the molecular absorption coefficients for the gaseous absorbers and  $P$  is the fraction of the gaseous absorption in the cloud, which is affected by the photon path distribution. The fraction will generally be different for water vapor,  $O_4$ , and the well-mixed gases like  $O_2$ , but this is neglected here because our goal is to estimate liquid and ice properties and to simply remove the gaseous absorption signals. We generally do not retrieve the water vapor fraction parameter, but have found from analyses of simulated spectra that under purely liquid, single-layer, homogeneous clouds, we are often able to accurately estimate the fraction of the total vapor column that resides in the cloud layer. Equations (3) and (4) are derived from the radiative transfer equivalence theorem [Van de Hulst, 1980]

$$I = I_0 \int_0^{\infty} p(l) \exp(-l\gamma) dl, \quad (5)$$

where  $p(l)dl$  is the photon path distribution, assumed here to be

$$p(\alpha, \langle l \rangle; l) = \frac{1}{\Gamma(\alpha) (\langle l \rangle / \alpha)^\alpha} l^{\alpha-1} \exp \left[ -\frac{\alpha l}{\langle l \rangle} \right] \text{ for } l > 0 \quad (6)$$

[Marshak *et al.*, 1995], and where  $\alpha$  is a parameter related to the variance (var) of the distribution by

$$\alpha = \frac{\langle l \rangle^2}{\text{var}(l)}. \quad (7)$$

We do not alter the distribution to prohibit paths of less than 1 air mass, as has been done by some authors [Min and Clothiaux, 2003]; however, we remain consistent in our analysis of calculated and measured spectra so the presented comparisons and retrievals are without bias. The choice of the specific distribution form, however, can affect the way in which measurement errors propagate into retrieval errors and can affect retrieval estimates. In addition to examining the values of  $\alpha$  itself, we will sometimes consider the more physical quantity, which we will call  $L^*$

$$L^* = \frac{\langle l^2 \rangle^{\frac{1}{2}}}{\langle l \rangle} = \sqrt{\frac{\alpha + 1}{\alpha}}, \quad (8)$$

where  $\langle l \rangle$  is the mean path length and  $\langle l^2 \rangle$  is the second moment of the path distribution.

[16] Constant terms  $b$  and  $c$  are included in equation (2) in order to eliminate the sensitivity of the retrievals to any linear or quadratic spectral change with wavelength, while the  $a$  term makes the analysis insensitive to constant-factor signal changes. Thus the analysis process gains information from more highly spectrally structured signatures rather than from slowly varying signals with wavelength that can be due to Rayleigh or aerosol extinction. So while aerosol and molecular scattering effects can have potentially large effects on dual- or several-wavelength cloud retrievals for thin clouds [e.g., King *et al.*, 1997], our technique avoids much of this problem.

[17] The retrieval problem is linearized so that the retrieved ratio,  $I_f/I_b$ , can be defined by

$$y = \frac{I_f}{I_b} = \mathbf{Kx}, \quad (9)$$

where  $\mathbf{x}$  is the vector of retrieved parameters and  $\mathbf{K}$  is the Jacobian matrix. The  $(i + 1)$ th iteration for the retrieved parameters is given by

$$\mathbf{x}_{i+1} = \mathbf{x}_i + \mathbf{S}_a \mathbf{K}_i^T (\mathbf{K}_i \mathbf{S}_a \mathbf{K}_i^T + \mathbf{S}_\varepsilon)^{-1} [y - \mathbf{F}(\mathbf{x}_i) + \mathbf{K}_i (\mathbf{x}_i - \mathbf{x}_a)], \quad (10)$$

and the covariance matrix of the retrieved parameters is given by

$$\hat{\mathbf{S}} = \mathbf{S}_a - \mathbf{S}_a \hat{\mathbf{K}}^T (\mathbf{S}_\varepsilon + \hat{\mathbf{K}} \mathbf{S}_a \hat{\mathbf{K}}^T)^{-1} \hat{\mathbf{K}} \mathbf{S}_a, \quad (11)$$

where  $\mathbf{S}_a$  is the a priori covariance matrix and  $\mathbf{S}_\varepsilon$  is the measurement covariance matrix [Rodgers, 2000]. One

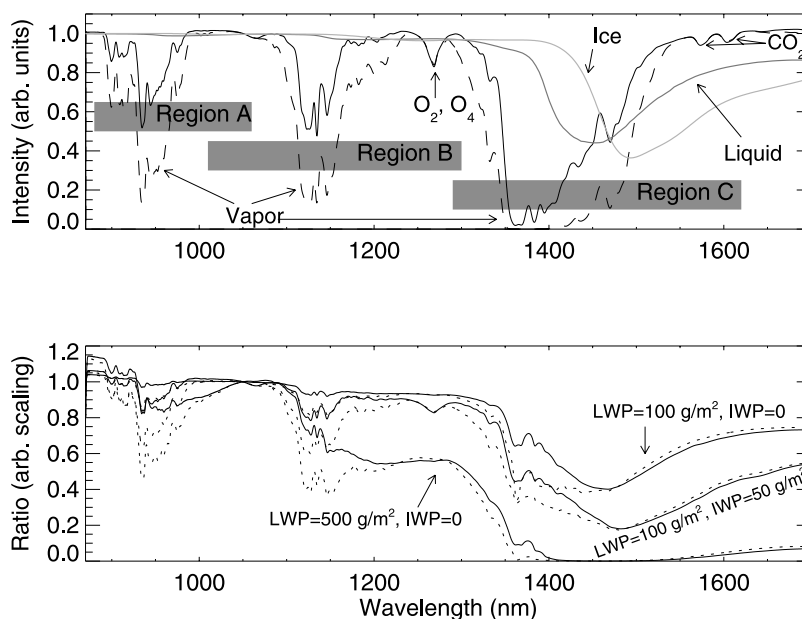


**Figure 1.** (top) Spectral ranges of the three retrieval bands considered. Calculated direct transmission spectra through bulk liquid and ice of 0.25 mm thickness along with clear-sky zenith normalized radiances are shown. (bottom) Calculated zenith-sky spectral ratios under pure liquid or liquid and ice clouds assuming a liquid cloud background containing 20 g/m<sup>2</sup> liquid water path (LWP). Both panels include calculations for low (solid) and high (dashed) water vapor cases.

alteration in using equation (10) is that the value of  $\alpha$  is held fixed for the first few iterations because of convergence problems if it is allowed to adjust before the other retrieval parameters are close to converging. The experimentally determined measurement variance (diagonal components of  $S_e$ ) is given by

$$\text{Var}_i = \left(3.1 + \sqrt{0.003n_c}\right)^2, \quad (12)$$

where  $n_c$  is the number of counts; the off-diagonal covariance terms are assumed to be 0. In retrievals from theoretical spectra, we use this same parameterization by applying a scaling factor between calculated intensity and counts assumed so the maximum modeled zenith counts (under the brightest cloud) is approximately 15,000 (out of a maximum of 65,536). This scaling factor is somewhat arbitrarily chosen, as the integration time can be altered within reasonable bounds for atmospheric measurements (i.e., so counts are large enough to detect the signal, but not so large that the signal is saturated) to optimize the observed signal. It leads to count numbers up to three times smaller than those measured under comparable clouds in Barrow on the day presented in section 4.

[18] The spectral absorption of the three water phases in our three analysis wavelength regions is shown in the top panel of Figure 1; the direct transmission through a layer of bulk liquid and ice is shown along with the clear sky downwelling surface radiances, whose absorption is dominated by water vapor. The surface zenith radiances for three cloudy atmospheres containing a range of LWPs divided by the radiances for a cloudy atmosphere containing a LWP of 20 g/m<sup>2</sup> are shown in the bottom panel. The liquid cloud layers are prescribed to be homogeneous between 1

and 2 km, while the homogeneous ice cloud layer is between 7 and 8 km. Comparing the top and bottom panels, the unique signatures of the three water phases are apparent and suggest promise for differentiating the absorption signals. Each spectral region also exhibits overlap of the water phases that can lead to errors in retrievals due to uncertainties in the atmospheric state, inaccuracies of the absorption cross sections, and other modeling errors. The significance of the overlap to the retrieved parameters depends on the atmospheric conditions, the specific wavelength region used in the analysis, the details of the retrieval method, as well as the particular retrieved parameter. As demonstrated in the top panel, the potentially greater interference of higher precipitable water vapor (PWV) is suggested by the noticeable contribution of vapor absorption at wavelengths even longward of the peak in the liquid absorption for the high PWV case. However, it is also clear from the bottom panel that including cloudy-sky radiances as a background spectrum in equation (2) can substantially reduce the effect of vapor errors on the retrieval of liquid and ice by canceling out much of the vapor signal. Both panels also illustrate how these wavelength ranges can provide useful cloud information for a wide range of optical thicknesses. As will be shown in section 3, Region C is sensitive to absorption due to LWPs of only a few g/m<sup>2</sup>, while Region A still provides information for thick clouds with LWPs of over 1000 g/m<sup>2</sup> [see also Daniel et al., 2002].

### 3. Retrieval Sensitivities

[19] In this section we quantify our ability to estimate PLWP, PIWP, photon path distribution width, and cloud liquid and ice temperatures using the three spectral regions shown in Figure 1. Specifically, the extent to which random

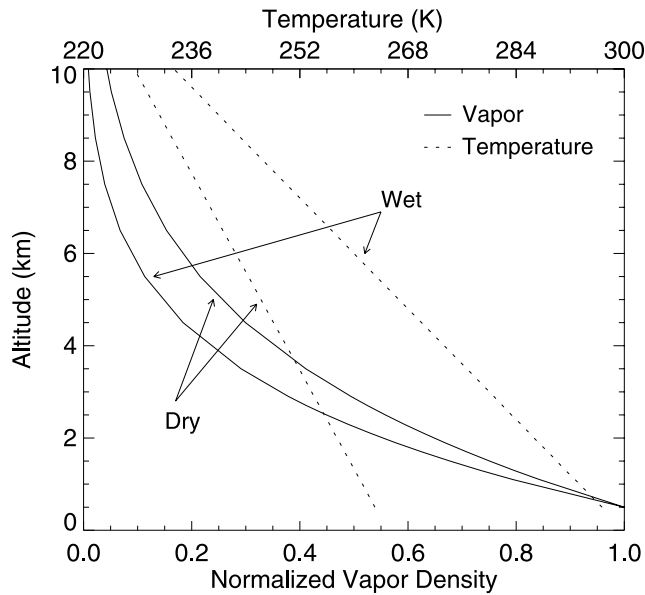


**Figure 2.** Temperature and normalized water vapor density profiles for the dry and wet water vapor cases.

measurement noise and other systematic errors can adversely affect the retrieved quantities is examined. An assumed set of atmospheric conditions is used in the radiative transfer forward model to simulate radiance spectra for the ground-based zenith-viewing observations for a range of cloud LWPs and IWPs. These spectra are then analyzed in each of the wavelength regions to make clear the strengths and weaknesses of each band under varying conditions. In section 4, analyses are also performed using Regions B and C simultaneously (Region B/C).

[20] Processes considered for their ability to induce systematic retrieval errors include drifts in the dark current of the spectrometer, uncertainties in photon path distribution widths (when not retrieved), the fraction of vapor assumed

to be in the cloud, cloud liquid temperatures, cloud droplet effective radii (due to spectral shape changes in the liquid cross section), and amounts and distributions of water vapor. The surface albedo will have some effect on relating PLWP to LWP and will be mentioned briefly in section 4 when we convert PLWP estimates from measurements to LWP values. The effect of vapor distribution uncertainty is assessed by considering warm (wet) and cold (dry) atmosphere cases, with surface temperatures of 300 K and 265 K, respectively, and with lapse rates of 6.7 K/km and 3.8 K/km, respectively, in the lowest 12 km of the atmosphere. In both cases the relative humidity profile is assumed constant at 60%. The temperature distribution and the resulting vapor profiles for the warm and cold cases are shown in Figure 2. The vapor number density profile is normalized to 1 in the lowest layer so the profile variation is apparent. The warm, wet case has a vertical water vapor column typical of July soundings taken in Norman, Oklahoma, from 1998 through 2003 (<http://raob.fsl.noaa.gov>), corresponding to about 37 mm of precipitable water, and the cold, dry case is typical of October soundings in Barrow, Alaska, corresponding to about 5 mm of precipitable water. Errors in the assumed absorption coefficients of the three water phases, themselves, will also lead to errors in all of the retrieved quantities, but will not be assessed here because arbitrary changes in these cross sections can yield inaccuracies in PLWP and PIWP with no limit in magnitude, depending on the size of the prescribed changes and how they are applied spectrally.

### 3.1. PLWP and PIWP

[21] The ratios of the retrieved PLWPs to the correct values for clouds consisting of various LWPs for the low water vapor case are shown in the top panel of Figure 3 for each of the retrieval spectral regions. For example, a value of 1.2 implies that the retrieved PLWP is 20% too high. The lower x-axis shows the approximate values for the PLWP corresponding to these prescribed LWPs for clouds characterized by an  $r_{eff}$  of 10  $\mu\text{m}$ . All cloud parameters, except the

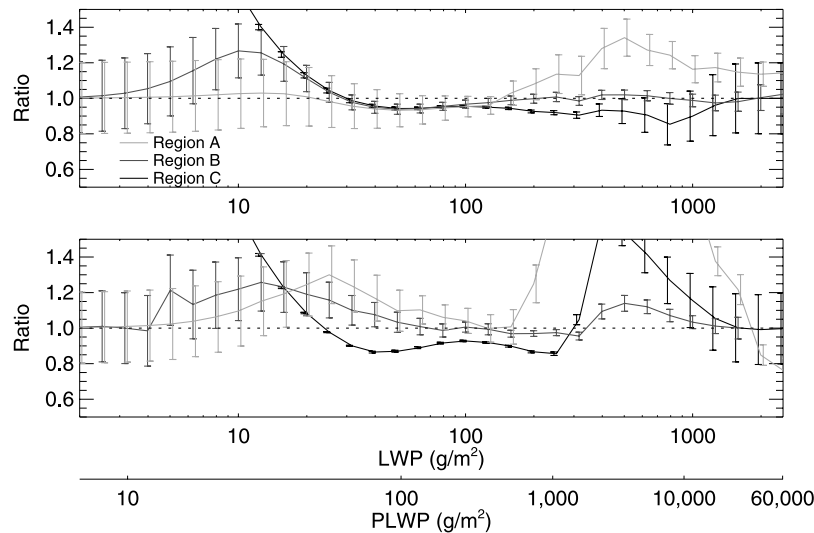


**Figure 3.** Ratios of retrieved path-integrated liquid water path (PLWP) relative to correct values for the three retrieval regions when using (top) a cloudy-sky background and (bottom) a constant background. Error bars represent a single standard deviation due to measurement noise.

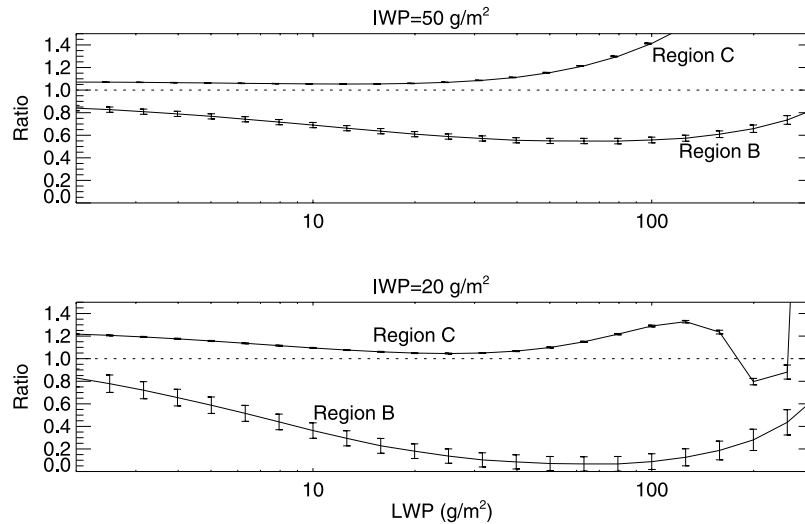


**Figure 4.** Ratios of retrieved path-integrated ice water path (PIWP) relative to the correct values for an overlying ice cloud with an IWP of (top)  $50 \text{ g/m}^2$  and (bottom)  $20 \text{ g/m}^2$ , using Regions B and C.

fraction of vapor in the cloud, are included in the retrieval process, and a calculated background spectrum with a LWP of  $43 \text{ g/m}^2$  is used. The error bars represent the  $1-\sigma$  retrieval errors due to random measurement noise and the prescribed 20% uncertainty in the a priori value; hence it is only when the estimated error falls below this 20% level that information is gained from the simulated measurement. The dependence of the retrieval uncertainties on the spectral analysis region is evident. As indicated by its smaller error bars, the PLWP retrieval from Region C demonstrates much greater sensitivity to LWP absorption under thinner clouds. This is owing to the larger liquid cross section in Region C. Regions A and B lead to smaller errors for thicker clouds, however, as  $\tau_{\text{abs}}$  of Region C increases to the point that there is little signal remaining.

[22] The bottom panel shows the same quantities as the top panel when using a spectrally constant background. The benefit of including a background spectrum is apparent from the degraded accuracy of the retrievals when using the constant background, particularly for  $\text{LWP} > 100 \text{ g/m}^2$ . The background, cloudy-sky spectrum can have the effect of reducing the vapor signal relative to the liquid signal and can permit more accurate retrievals, consistent with Figure 1. Thus, picking a background with a comparable vapor absorption to the foregrounds of interest is preferable. The other notable point is that the Region C retrievals under very thin clouds ( $\tau_{\text{scat}} < 2$  or  $\text{LWP} < \sim 13 \text{ g/m}^2$  for  $r_{\text{eff}} = 10 \mu\text{m}$ ) demonstrate a significant high bias. It is implicitly assumed in our use of the equivalence theorem (equation (5)) that the scattering radiative properties (e.g., asymmetry factor and scattering optical depth) at all wavelengths in the particular band considered are constant. While this is generally a reasonable assumption, it becomes invalid under optically thin clouds, when the correlation between  $g$  and  $\tau_{\text{scat}}$  with  $\tau_{\text{abs}}$  leads to significant intensity changes that have the same spectral signature as absorption. In the optically thicker part of this  $\tau_{\text{scat}}$  regime, the interpretation of the data is dependent on cloud droplet effective size, with an opportunity for meaningful PLWP and LWP estimates if the radius can be accurately estimated. Under optically thinner clouds (when

the single scattering approximation is valid) no direct PLWP information is contained in the measurements because the depth of the spectral feature is controlled by  $\omega$ . This regime can also be used to advantage, however, as information about the size of cloud particles can be more directly obtained [Langford *et al.*, 2005]. The retrievals from the other two spectral regions do not exhibit this effect as much because they do not contain enough information under such thin clouds to yield a PLWP estimate that deviates substantially from the a priori value. More discussion of the PLWP sensitivities to various retrieval assumptions can be found in Appendix A.

[23] In Figure 4, PIWP retrievals are shown for the same cloud LWP range as in Figure 3, but with an added ice layer between 7–8 km of  $50 \text{ g/m}^2$  (top panel) and  $20 \text{ g/m}^2$  (bottom panel) IWP to explore the effect of an overlying cirrus layer. The results are similar to the pure liquid case in that Region C provides better ice estimates than Region B under clouds with low IWP. Also, as with the liquid retrievals, the breakdown of the assumption of constant scattering with wavelength accounts for a large part of the bias for the thinner,  $20 \text{ g/m}^2$  IWP cloud. As the clouds get thicker the effect of having a substantially larger liquid absorption than ice absorption leads to unacceptably large errors in PIWP. This effect applies to both liquid and ice; if there is a substantially greater ice (liquid) absorption than liquid (ice), the PLWP (PIWP) will most likely be erroneous owing to the effects of measurements noise and retrieval modeling errors, whose importance is enhanced by the overlap of the absorption features.

[24] In general, PLWP retrievals can be made accurately for a wide range of pure liquid clouds containing LWPs from  $< 20 \text{ g/m}^2$  to over  $1000 \text{ g/m}^2$  with the appropriate choice of analysis spectral band, retrieval parameters, and a cloudy sky background that minimizes errors in fitting water vapor absorption. Good estimates of PIWP can also be made in cases where the liquid present is not substantially larger than the amount of ice. The presence of high PWV amounts, having a large amount of water in another phase, and uncertainties in the value of the photon path

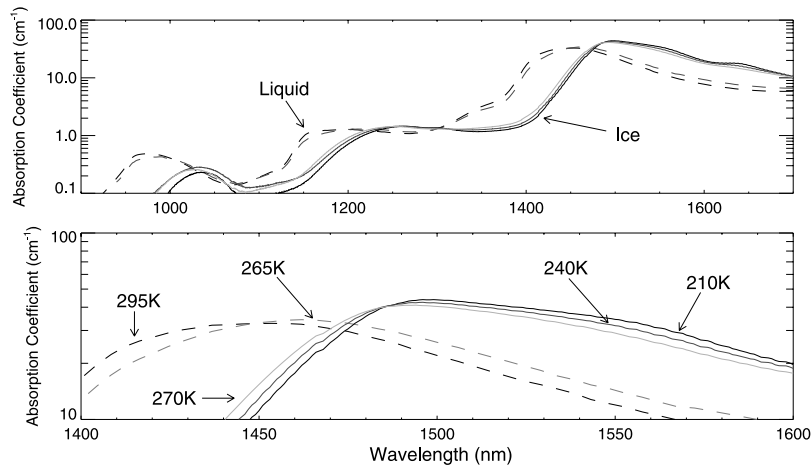


**Figure 5.** Liquid absorption coefficients for 265 K and 295 K taken from *Kou et al.* [1993]. Ice absorption coefficients for 210 K, 240 K, and 270 K taken from *Grundy and Schmitt* [1998]. The bottom panel enlarges the wavelength region from 1.4 to 1.6  $\mu\text{m}$ .

distribution parameter (Appendix A) represent some of the most significant factors that can potentially degrade the retrieval.

### 3.2. Liquid and Ice Temperatures

[25] Liquid and ice temperatures are retrieved using temperature-dependent shifts (as well as the slight shape variations) of the absorption cross sections with wavelength. Absorption coefficients for bulk liquid, taken from *Kou et al.* [1993], and for bulk ice, taken from *Grundy and Schmitt* [1998], are shown in Figure 5. The shift of the absorption spectral features to longer wavelengths with decreasing temperature occurs for both liquid and ice. The use of these spectral shifts requires that there be sufficient absorption (or spectrally coincident scattering spectral signatures) for the spectral shift to be detectable in the presence of absorption due to the other water phases.

[26] Liquid temperatures are estimated from calculated spectra of purely liquid clouds characterized by a liquid

temperature of 260 K assuming an a priori temperature of  $270 \pm 10$  K. The top panel of Figure 6 shows the retrieval of cloud liquid temperature using the three wavelength bands for the low atmospheric water vapor case. The most sensitive band (Region C) performs best for cloud LWPs less than a few hundred  $\text{g/m}^2$ , with the other two bands demonstrating superior retrievals for the thicker clouds. Liquid temperatures accurate to within about 5 K can be obtained from at least one of the wavelength regions in low water vapor cases for clouds with LWPs greater than about  $10 \text{ g/m}^2$ ; results are substantially worse in the high vapor cases owing to the increased spectral overlap between the vapor and liquid absorption. Because of the significance of the vapor/liquid overlap, the most important factor in obtaining accurate temperature estimates in even low vapor cases is to use a cloudy-sky background in the retrieval. Including ice temperature in the retrieval also leads to noticeably worse results for liquid temperature.

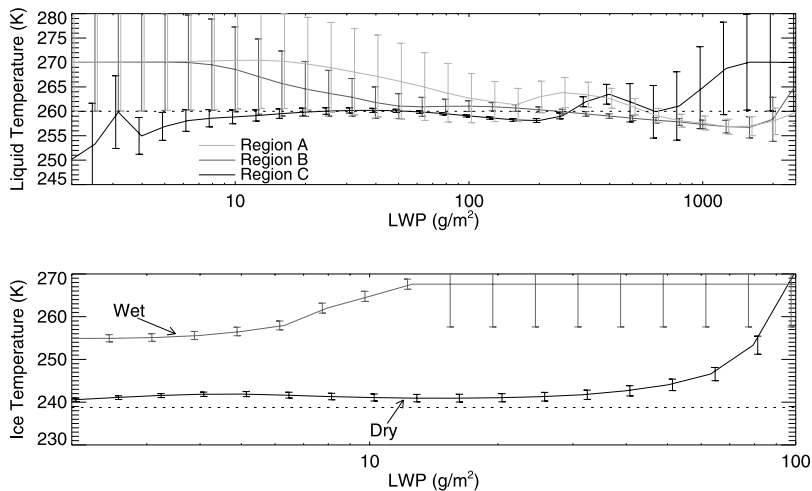


**Figure 6.** (top) Retrieved liquid temperatures for purely liquid clouds of various LWPs compared to the correct temperature of 260 K. (bottom) Ice temperature retrievals using Region C for wet and dry water vapor cases compared to the correct temperature of 239 K.

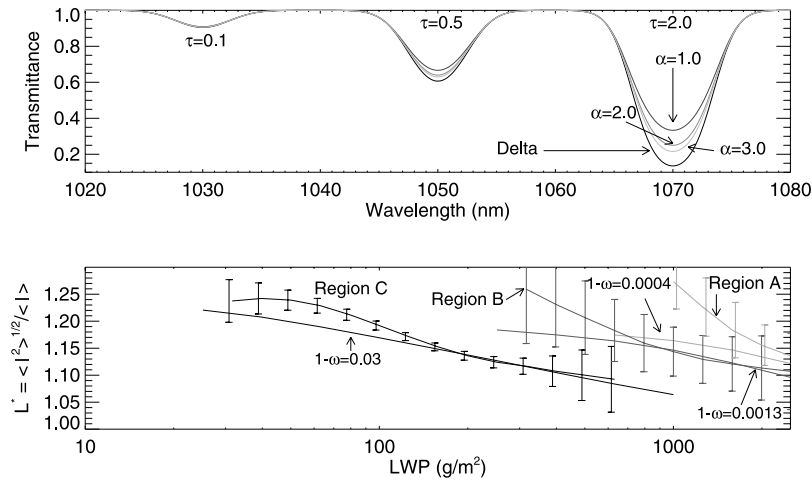


**Figure 7.** (top) Calculated transmission curves for absorption features of three optical depths (0.1, 0.5, 2.0) assuming various photon path distribution widths. (bottom) Directly calculated variation in  $L^*$  as a function of LWP for three single scattering albedos. Superimposed are values of  $L^*$  retrieved from synthetic spectra for the three spectral regions.

[27] Ice temperature retrievals for cloud simulations with a  $50 \text{ g/m}^2$  IWP and a range of LWPs in high and low water vapor cases are shown in the bottom panel of Figure 6. The ice is located in a homogeneous layer from 7–8 km with a temperature of 239 K. Ice temperature retrievals in the dry vapor case are accurate to within about 5 K for LWPs less than about  $50 \text{ g/m}^2$ , but substantially worsen as the liquid absorption increases and begins to obfuscate the ice spectral feature. The removal of  $\alpha$  and liquid temperature from the retrieval does not improve the results, and actually slightly degrades the retrieved ice temperatures. As with the liquid temperature retrievals, ice temperature retrievals are more problematic in higher vapor conditions.

### 3.3. Photon Path Distribution

[28] Diffuse photons transmitted through a cloud will have traveled a variety of distances and paths before reaching the observer, whether the observer is below or above the cloud. If the absorption due to the distribution of these photons is measured, the average photon path length through the absorber can be inferred unambiguously providing the absorption is optically thin. Once photon paths begin to experience optically thick absorption, the longer paths, being largely attenuated, contribute less to the intensity measurements than do the shorter paths, and the mean absorption is no longer uniquely related to a mean photon path length but depends on the photon path distribution. It is this dependence that we exploit to obtain path distribution information.

[29] As mentioned in the introduction, numerous papers have addressed the photon path distribution and its effects on reflected and transmitted solar radiation, with information garnered from oxygen A-Band and water vapor absorption features. Here we use the liquid water absorption spectrum to quantify path distribution information for purely liquid clouds; however, water vapor does contribute to our distribution estimates because we consider only a single path distribution within the cloud, rather than one for vapor and another for liquid absorption. The effect of vapor on the retrieval of  $\alpha$  (equation (6)) could also be reduced by

only analyzing the wavelengths longward of the liquid absorption maximum, where vapor has a much reduced impact. In a homogeneous cloud, the path information should be identical for a gaseous absorber that has a constant number density inside the cloud and for cloud liquid. However, inhomogeneities inside the cloud can lead to differences. In particular, the use of oxygen or water vapor will be sensitive to the physical length the photons travel through the cloud and the atmosphere, while liquid absorption will provide information about the statistics of photon/particle events, as it is only these events, and not the geometric distance between them, that lead to liquid absorption. The differences in the information contained in the gaseous and liquid absorption potentially could be used to probe the three-dimensional inhomogeneous nature of clouds.

[30] The manner in which various characteristic  $\alpha$ s can affect an absorption feature is shown in the top panel of Figure 7. The three absorption features shown have prescribed peak  $\tau_{\text{abs}}$  of 0.1, 0.5, and 2.0 with Gaussian line shapes characterized by a FWHM of 5.3 nm. The curve labeled “Delta” represents the transmittance of a direct beam of light, whose path distribution is a Dirac delta function, through the absorber. The other curves illustrate the transmittance for the same optical depths but with various choices of the parameter  $\alpha$  in the path distribution function given by equation (6). Variations in the value of  $\alpha$  lead to changes in the transmittance curves that become greater as the optical depths increase and the photon path distribution broadens. These changes are manifested as changing spectral shapes and reduced depths of the absorption features relative to a delta function distribution. This implies that  $\alpha$  information can only be accurately obtained when the absorption optical depths are thick enough to provide the needed sensitivity to  $\alpha$ , but not so thick that the signal is saturated. Values of  $L^*$  (equation (8)), directly calculated from DISORT for liquid clouds, are shown in the bottom panel of Figure 7 as a function of LWP for three different coalbedos that are consistent with the coalbedos of

the three liquid absorption band centers for an  $r_{eff}$  of 10  $\mu\text{m}$ . The calculations of  $L^*$  are performed from the calculated transmission at a single wavelength assuming various values for  $\tilde{\omega}$ ; details of this calculation are described in the first part of Appendix B. The curves for each band are only shown for the LWP range most sensitive to  $L^*$ . The dependence of  $L^*$  on LWP and  $\tilde{\omega}$  is evident, with the latter potentially leading to difficulty in estimating a “true” value of  $L^*$ , or  $\alpha$ , since  $\tilde{\omega}$  varies across a single absorption band. The  $L^*$  retrievals for the dry atmospheric calculated cases are also shown for each of the three wavelength regions, along with their 1- $\sigma$  error bars due to measurement noise. The retrieved  $L^*$  values agree well with the directly calculated values. One potentially important source of error is a spectrally constant offset in the foreground (or background) spectrum. Such an offset can occur owing to stray light in the spectrometer or to variations in the detector temperature. Because the information for estimating the path distribution width is contained in the optically thick spectral region, and is thus characterized by lower counts, it is not surprising that an error in zero-count level could be problematic. When the calculated foreground spectrum is increased by 10 counts at all wavelengths, for example,  $\alpha$  changes by less than 0.25 for Region C for LWPs between about 40 and 160  $\text{g/m}^2$ , but changes substantially outside this range. The value of 10 counts is a reasonable choice because, as a fraction of the signal, it is similar to the amount of dark drift in the observations discussed in section 4. Additional details relating to both the calculation and the retrieval of photon path distribution information are found in Appendix B.

### 3.4. Modeling Summary

[31] Each of the previously discussed cloud parameter estimates exhibit different degrees of sensitivity to various aspects of the retrieval process, but there are several general conclusions that can be drawn. Perhaps most important, it is usually beneficial to include a measured spectrum, for which the atmospheric state is known, as the background spectrum in the analysis. This background is chosen to reduce the sensitivity of the retrieved quantities to the presence of water vapor and thus to errors in correctly modeling vapor; the choice becomes more important when analyzing measurements obtained in a moist environment. Second, the particular parameters included in the analysis can have an important effect on the accuracy of other retrieval estimates. In general, if the absorption band is not optically thick ( $\tau_{abs} < \sim 1$ ) it is preferable to fix, rather than to retrieve,  $\alpha$ . Similarly, if it is known that the clouds are of a single phase (liquid or ice), it is generally advantageous to remove the phase that is not present from the analysis. When these recommendations are followed, the calculations suggest that accurate estimates can be made of PLWP, PIWP, liquid and ice temperature, and photon path distribution width under many cloud conditions.

## 4. Observations

[32] Zenith-looking spectral observations of scattered sunlight were made between 12 September and 21 October 2004 in Barrow, Alaska, at the DOE ARM facility (71°19'N, 156°37'W). This observational period was chosen

to coincide with the mixed-phase Arctic cloud experiment (M-PACE) intensive measurement campaign, conducted at a time when clouds consisting of liquid and ice phases were climatologically expected. A more extensive examination of the data taken during this measurement period, as well as a detailed comparison to the measurements of other collocated instruments will be provided in a subsequent paper. Here, we present our retrievals from data taken on 14 September to illustrate the application of our retrieval technique to measurements. We also compare these results to estimates from coincident and collocated measurements made by the ARM MWR, MMCR, and AERI. Throughout most of this day, frozen precipitation was falling from these clouds.

[33] The fixed-grating, commercially purchased spectrometer used to acquire the spectral measurements covers the wavelength range from about 0.9 to 1.65  $\mu\text{m}$ , uses an InGaAs detector, and has an approximate spectral resolution of 4–5 nm (see Appendix C for additional instrument details and analysis sensitivities to these characteristics). It is similar to the instrument used by *Langford et al.* [2005] to measure subvisible cirrus particle sizes, except that this one has half the number of diodes and a spectral resolution about twice as coarse. A fixed aperture and fiber feed restricted the full angle field-of-view to about 10°, and the detector was cooled to  $-10^\circ\text{C}$  during the deployment. The integration period for each spectrum throughout this day was 2.0 s, with retrievals shown here performed on 10 co-added spectra to reduce computational time. Some additional considerations for analyzing these measurements as opposed to the simulated spectra of section 3 are also discussed in Appendix C.

[34] The MWR has two channels, 23.8 and 31.4 GHz, with fields-of-view of 5.9° and 4.5°, respectively. The retrieval technique employs the monoRTM absorption model [*Clough et al.*, 2005] with atmospheric temperature, pressure, and vapor profiles taken from radiosonde data acquired on 13 September. It is often stated that the microwave LWP error is about  $\pm 30 \text{ g/m}^2$  [*Morris*, 2005]; however, with radiosonde information not available on 14 September, the uncertainties here are likely higher than this.

[35] The AERI is a ground-based interferometer that measures downwelling atmospheric radiance from 400–3000  $\text{cm}^{-1}$  (2.5–3.3  $\mu\text{m}$ ) at approximately 1  $\text{cm}^{-1}$  spectral resolution. During M-PACE it was run in a “rapid sample” mode, whereby 12-s averaged atmospheric radiance spectra are collected every 30–40 s. A principal component analysis noise filter is used to reduce the uncorrelated random error [*Turner et al.*, 2006], and the optical depth and effective radius were then retrieved using a mixed-phase retrieval algorithm [*Turner*, 2005]. The clouds were specified to contain only liquid, however, because the precipitable water vapor was too large to permit both the liquid and the ice microphysical properties to be retrieved simultaneously. The AERI retrievals of cloud properties here are generally limited to clouds with optical depths less than approximately 6.

[36] The MMCR operates at 35 GHz with a beam width of 0.3° [*Moran et al.*, 1998] and possesses the sensitivity to detect most liquid and ice clouds. Through a combination of MMCR, MWR, radiosondes, and other supporting measurements, cloud phase can be determined

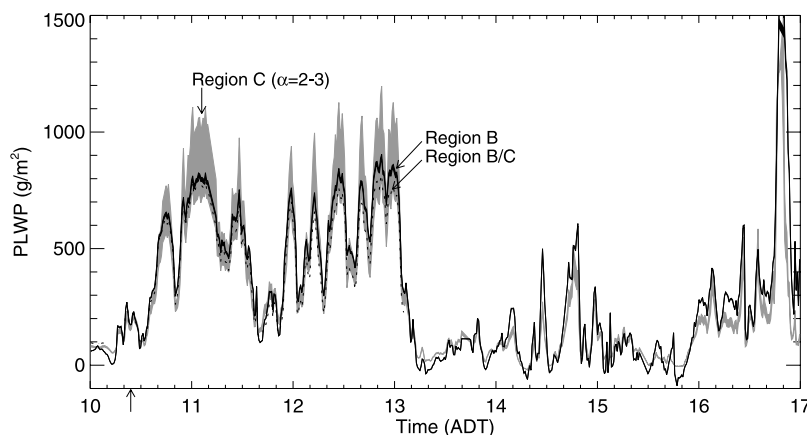


**Figure 8.** PLWP retrievals for measurements taken on 14 September 2004 at Barrow, Alaska. Region B (black region) and Region C (grey region) retrievals are calculated with  $\alpha$  fixed from 2 to 3. Combined Region B/C results when including  $\alpha$  in the retrieval are shown before 1300 ADT. Arrow shows the time the background spectrum was taken.

[Shupe *et al.*, 2005]. The IWC profile is estimated using the simple relationship

$$IWC = aZ^b, \quad (13)$$

where  $a$  and  $b$  are constants that vary with location, season, cloud, etc, and  $Z$  is the radar reflectivity. On the basis of a detailed analysis of measurements made during the Surface Heat Budget of the Arctic Ocean (SHEBA) project [Shupe *et al.*, 2005], we assume values for  $a$  and  $b$  of 0.0766 and 0.63, respectively. The integrated IWP estimates from the radar must be considered primarily qualitative owing to the uncertain effects of ice crystal habit and crystal effective size in deriving the relationship between IWC and  $Z$ ; Shupe *et al.* [2005] suggest that Arctic radar-based IWP retrievals of this nature can be uncertain by as much as a factor of two. More information regarding each of these ARM instruments can be found at <http://www.arm.gov>.

[37] Retrieved PLWP values for 14 September from 1000 to 1700 ADT (Alaska Daylight Savings Time; GMT-8) are shown in Figure 8. The average of 10 cloudy-sky spectra taken from 10:24:05 to 10:24:25 ADT was used as the background spectrum for all spectral retrievals shown in this figure. The grey shaded region represents the retrieved PLWP range from Region C with  $\alpha$  fixed between 2.0 and 3.0, and demonstrates that the photon path distribution width has a major effect on the PLWP retrievals for PLWP values more than a few hundred  $\text{g/m}^2$  in this sensitive band. This illustrates the necessity of retrieving the value of  $\alpha$  when  $\tau_{\text{abs}}$  in the analyzed wavelength region gets large. In contrast, the same assumed range for  $\alpha$  plays a minor role in Region B retrievals throughout the day (black region). When  $\alpha$  is included in the retrieval process using Region B/C, the PLWP results are similar to the Region B results during the periods of relatively high PLWP. In the afternoon, when the clouds became optically thinner, the observations demonstrate little sensitivity to  $\alpha$  for much of the period; during this time the Region B/C results frequently do not converge and are not shown.

[38] If homogeneous, plane-parallel liquid clouds are assumed, a nearly unique correlation between the retrieved

PLWP values and LWP can be calculated as a function of radius, solar zenith angle, and surface albedo. DISORT2.0 [Stamnes *et al.*, 1988] was used to calculate (at  $1.4 \mu\text{m}$ ) the cloud path enhancements shown in Figure 9 that relate LWP and PLWP. While high-frequency variations in the spectral structure of the surface albedo and variations in the LWC profile [Platnick, 2000] can affect this relationship, we neglect these effects here. Between about 50 and  $100 \text{ g/m}^2$  the path enhancement increases substantially with LWP for these  $r_{\text{eff}}$ 's, and the greater importance of knowing  $r_{\text{eff}}$  is evident. It is also clear that changes in  $r_{\text{eff}}$  have little effect on the path enhancement for the optically thinner clouds, leading to less ambiguity due to radius in estimating LWP from PLWP (above the optically thin limit). The change in path enhancement due to a decrease of the surface albedo to 0.0 from 0.2

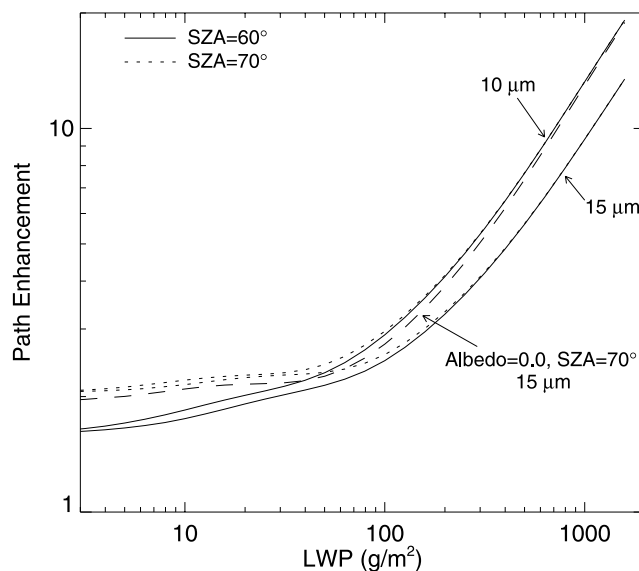


**Figure 9.** Calculated cloud path enhancements assuming an  $r_{\text{eff}}$  of 10 and  $15 \mu\text{m}$  for solar zenith angles of  $60^\circ$  (solid) and  $70^\circ$  (dotted) solar zenith angles. In all cases except for the dashed curve the surface albedo is prescribed to be 0.2.

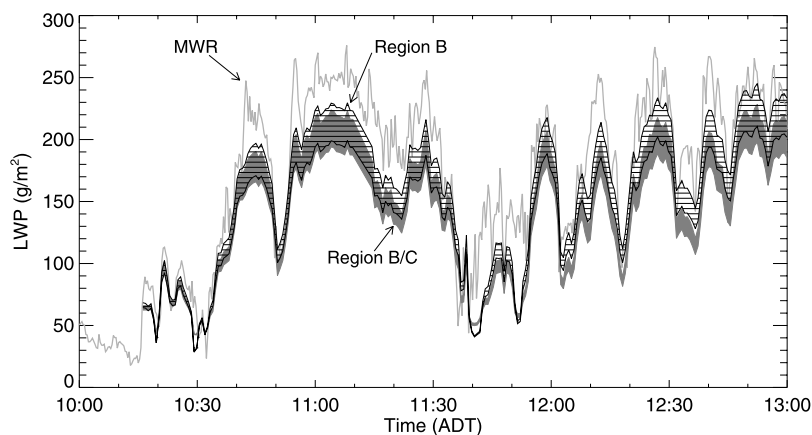


**Figure 10.** Spectrally retrieved LWP estimates using Region B and combined Region B/C are compared to LWP estimates from the Atmospheric Radiation Measurement (ARM) microwave radiometer (MWR). The shaded LWP areas represent the range resulting from cloud droplet  $r_{\text{eff}}$  assumptions of  $10 \mu\text{m}$  (lower boundary) to  $15 \mu\text{m}$  (upper boundary).

(dashed versus dotted curve) peaks at slightly more than 7%, occurring at LWPs of  $50\text{--}200 \text{ g/m}^2$  for  $r_{\text{eff}} = 10 \mu\text{m}$ , with a substantially smaller effect under optically thicker clouds. It is expected that the albedo-caused uncertainty will be smaller than this in practice (excepting a spectral structure correlated with liquid or ice absorption) because at these wavelengths, the surface albedo over the ocean is likely only a few percent and the value over land across the entire wavelength range likely varies from about 0.05 to 0.25, with substantially less variation within each individual analysis band [Wendisch *et al.*, 2004]. However, if snow were present on the ground, as it is later in September during this campaign, the path enhancement change would be greater.

[39] These cloud path relationships are applied to the PLWP values for the Region B retrievals ( $\alpha = 2.0$ ) and the Region B/C retrievals in which  $\alpha$  was retrieved (Figure 8) to yield the LWP time series shown in Figure 10. The shaded and hatched regions represent the LWP ranges obtained assuming the cloud droplet  $r_{\text{eff}}$  range  $10\text{--}15 \mu\text{m}$  for these two cases. The values inferred using the  $10 \mu\text{m}$  assumption are represented by the lower boundary of the regions; the smaller radius leads to a larger  $\tau_{\text{scat}}$ , and thus a larger path enhancement for the same PLWP, which results in a smaller inferred LWP. Overall, the qualitative comparison between the MWR estimates and the spectrally retrieved LWP values is good throughout the period. Throughout most of the time period shown, when the MWR LWP values are greater than the spectral estimates, the spectral LWPs could be brought into agreement with the MWR curve by making a larger  $r_{\text{eff}}$  assumption than  $15 \mu\text{m}$ . A linear regression of the spectrally inferred LWP values using Region B ( $\alpha = 2.0$ ) and assuming an  $r_{\text{eff}}$  of  $15 \mu\text{m}$ , to the MWR estimates results in an intercept of  $-9 \text{ g/m}^2$ , a slope of 0.94 and an  $r^2$  correlation coefficient of 0.93.

[40] Because of the sensitivity of the relationship between PLWP and LWP to  $r_{\text{eff}}$ , if confidence could be placed on a particular MWR LWP estimate as well as on the spectrally retrieved PLWP value, a unique  $r_{\text{eff}}$  could be inferred. We propose that this combination of MWR and spectral measurements could be used to estimate  $r_{\text{eff}}$  during periods when

the LWP is not too low and when clouds are sufficiently plane-parallel. A ground-based technique such as this has the advantage that by using transmitted light, the retrieved radius should describe more appropriately the mean cloud  $r_{\text{eff}}$  than would reflected light, which would be more sensitive to cloud radius near the top of the cloud [Platnick, 2000]. Furthermore, it would require no absolute intensity calibration of the near-infrared spectrometer. Hence this technique could provide a relatively simple way to monitor  $r_{\text{eff}}$  changes from the surface and for extended periods of time. Of course, the accuracy of the  $r_{\text{eff}}$  retrieval will depend crucially on the PLWP accuracy, determined by factors discussed elsewhere in this paper, as well as the microwave LWP accuracy. The current inaccuracies of the MWR LWP values are likely to be substantial obstacles as they were in a similar approach to inferring  $r_{\text{eff}}$  using Multi-Filter Rotating Shadowband Radiometer (MFRSR) observations in conjunction with MWR LWP estimates [Min and Harrison, 1996; Min *et al.*, 2003].

[41] The LWP and PIWP retrievals for the time period 1300 to 1700 ADT are shown in Figure 11. During this period the clouds were generally characterized by lower LWPs than those shown in Figure 10. These ice and liquid retrievals are obtained from Region C ( $\alpha = 2.0$ ) by using a background spectrum calculated as the average of 10 cloudy-sky background spectra taken at 1311 ADT. This background was chosen for the analysis of this time period because the background taken in the morning leads to a large PIWP offset from zero throughout much of the afternoon for some applications of the retrieval method, even at times when the MMCR suggested no measurable ice was present. The LWP estimates (top panel) from the near-infrared measurements are compared to those of the MWR and AERI, where AERI retrievals with estimated  $1\text{-}\sigma$  uncertainties greater than  $15 \text{ g/m}^2$  have been excluded as have AERI data when the MMCR ice estimates are greater than  $25 \text{ g/m}^2$ . There is a short period near 1415 ADT when the near-infrared retrieval yields unphysical, negative PLWP values, which are coincident with positive PIWP measurements at a time when the MMCR suggests very little ice present. However, overall, the spectral near-infrared, AERI,

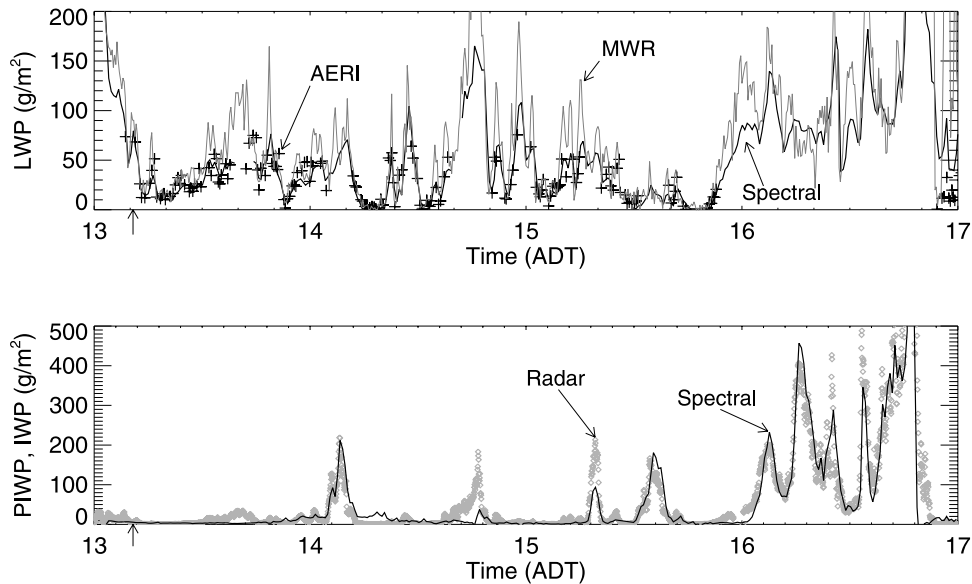


**Figure 11.** (top) Comparison of spectrally retrieved LWP from Region C with estimates from AERI observations (pluses) and from MWR observations. (bottom) Comparison of spectrally retrieved PIWP estimates with IWP estimates from the millimeter-wavelength cloud radar (MMCR). Arrows show the time the background spectrum was taken.

and MWR retrievals are in good agreement regarding the temporal variability throughout most of the afternoon. Linear regressions of the spectral LWP results against the MWR and AERI values result in intercepts of 15 and 2 g/m<sup>2</sup>, respectively, slopes of 0.57 and 0.86, respectively, and  $r^2$  correlation coefficients of 0.77 and 0.74, respectively. For this analysis with the AERI results, the associated spectrally inferred LWP values were determined by averaging all spectral LWP values obtained within 30 s of each AERI estimate.

[42] The spectrally retrieved PIWP values are compared to IWP estimates from the MMCR reflectivity measurements in the bottom panel of Figure 11. We do not attempt to convert PIWP to IWP here because of complications in accurately calculating the PIWP/IWP relationship that depend on, for example, ice crystal habit and the ice location relative to the liquid cloud layer. It is worth noting, however, that because the ice is generally below the liquid layer on this day according to the MMCR returns, if the path enhancement inside the ice layer is 1, due to the larger ice particles and the dominance of forward scattering, PIWP estimates would be equal in magnitude to IWP estimates.

Nevertheless, at least qualitatively, the near-infrared retrievals capture almost all of the cloud variability of IWP as measured by the MMCR, even in the presence of liquid absorption. The one exception is the peak near 1445 ADT, although a large detection with the MMCR along with a smaller near-infrared signal could be caused by a low-IWP cloud composed of particularly large ice crystals. Especially encouraging is that the liquid and ice comparisons perform well even during times when the clouds exhibited substantial amounts of both phases (e.g., 1600–1700 ADT). Noting the uncertainties in knowledge of the photon path as well as in the MMCR relationship between IWC and Z (equation (13)), a linear regression of the spectrally estimated PIWP against the radar IWP values results in an intercept of 6 g/m<sup>2</sup>, a slope of 0.8, and an  $r^2$  coefficient of 0.85. This suggests that the spectral technique, using data from a single near-infrared spectrometer, can be used to infer important cloud information for both single- and mixed-phase clouds.

[43] The cloud liquid temperatures from 1000 to 1300 ADT retrieved from Region B/C are presented in Figure 12 when including and not including ice in the retrieval analysis. There are no radiosonde data available

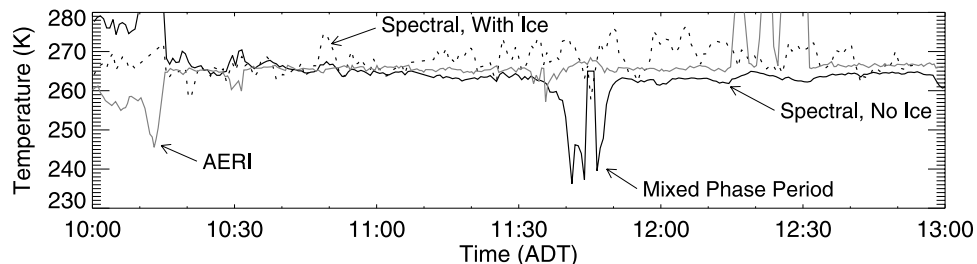


**Figure 12.** Liquid temperatures retrieved using combined Region B/C compared to AERI 11- $\mu$ m brightness temperatures. Results are shown for spectral retrievals performed with and without ice in the analysis.

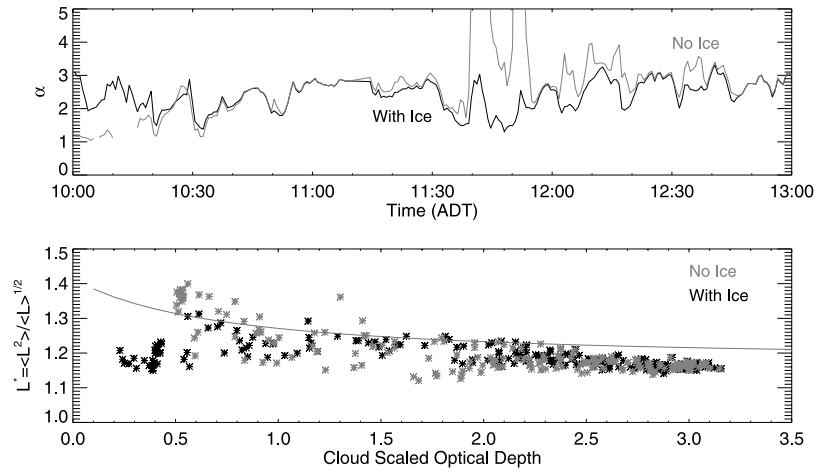


**Figure 13.** (top) Retrieved  $\alpha$  value when including and not including ice in the retrieval process. The  $1-\sigma$  uncertainty due to measurement noise in the  $\alpha$  estimates used to generate the bottom panel is smaller than 0.13. (bottom) Relationship between inferred  $L^*$  for these two cases with estimated scaled cloud optical thickness compared with theoretical diffusion limit calculation (line) from Davis and Marshak [2002]. The values of  $L^*$  between 1135 and 1150 ADT are not included in the bottom panel owing to the larger quantity of ice in the clouds.

with which to estimate cloud liquid temperature on this day, but a temperature estimate can be made by knowing that the cloud heights are generally 700–1000 m above the surface from the ARM micropulse lidar [Flynn, 2004], and that the surface temperature ranges from 270–274 K throughout the measurement period. This would suggest a cloud temperature somewhere between 260 and 270 K if a simple lapse rate of  $\sim 6\text{--}10$  K/km (wet-dry adiabatic) is assumed. The 11- $\mu\text{m}$  brightness temperatures measured by the AERI are consistent with this estimate and are also shown in the figure. Because the MMCR data suggest that the liquid portion of the cloud is thin ( $<100$  m), it is expected that the AERI brightness temperatures and the spectrally inferred temperatures should compare well when the AERI’s signal is saturated. The retrieval that does not include ice, but fixes it at  $0\text{ g/m}^2$ , generally provides a constant temperature estimate that agrees well with the AERI estimate for times other than the mixed-phase period between 11:30 and 12:00. The temperature retrieval when including ice demonstrates greater variability, with the temperature correlated with the amount of ice retrieved during the periods when little cloud ice was present. Although theoretical calculations suggested the success of retrieving temperature using Region C, in this case the use of Region C alone results in widely varying retrieved temperatures from 10:30 to 13:00 when not including and including ice in the retrieval of greater than 20 K and 40 K, respectively, even when the mixed-phase period is excluded. It is expected that modest errors in the wavelength registration, and thus in the shift and stretch retrievals, could lead to liquid temperature errors because the temperature is estimated from the wavelength shift in the liquid absorption cross section. This is not the cause of the temperature differences shown in Figure 12, however. While the temperatures differ by up to 10 K between the two Region B/C analyses (not including the period of substantial ice about 11:45), the shift and stretch differences are always less than 0.01 and 0.03 diodes ( $\sim 0.3$

and 0.09 nm), respectively. Because the laboratory water cross sections suggest a wavelength shift of roughly 3K/nm, these wavelength registration differences are much too small to account for the retrieved temperature differences.

[44] The retrieved values of the photon path distribution parameter  $\alpha$  for the time period 1000 to 1300 ADT are shown in the top panel of Figure 13. Region B/C is used because the  $\tau_{\text{abs}}$  for these clouds is in the range sensitive to changes in  $\alpha$  for this spectral region and the PLWP values are consistent with those obtained with Region B alone. After this period, as previously mentioned, the clouds become too thin to obtain meaningful estimates of  $\alpha$  except for a few time periods. Because of the correlation between  $\alpha$  and the liquid water temperature, these retrievals have been performed with liquid temperature fixed at 265 K. In one case, ice is included in the analysis (although there is little ice present throughout most of the time period) and in the other it is not; the  $\alpha$  retrievals demonstrate some sensitivity to this choice and the differences between the 2 estimates of  $\alpha$  from 12:00 and 12:40 are correlated with the amount of ice retrieved. During the 18 minute period beginning at 1136 ADT the  $\alpha$  values for the “no ice” case are suspect because of the ice present. In the bottom panel, we show the correlation between  $L^*$  and a measure of cloud optical depth,  $\tau'$ , excluding this mixed-phase period. The retrieved LWPs are scaled to  $\tau'$  by  $(1 - g) \tau$  assuming that the relationship between LWP and this quantity is given by

$$\tau' = 0.11 \times 0.13 \times LWP, \quad (14)$$

as would be expected with an effective radius of 15  $\mu\text{m}$  and  $g = 0.87$ . We do this to compare our measurement estimates of  $L^*$  ( $\langle I^2 \rangle^{1/2} / \langle I \rangle$ ) to the theoretical predictions from diffusion theory given by Davis and Marshak [2002]. The data demonstrate some scatter, especially when ice was included in the analysis, but compare reasonably well to the calculated values. The case in which ice is fixed to  $0\text{ g/m}^2$  in

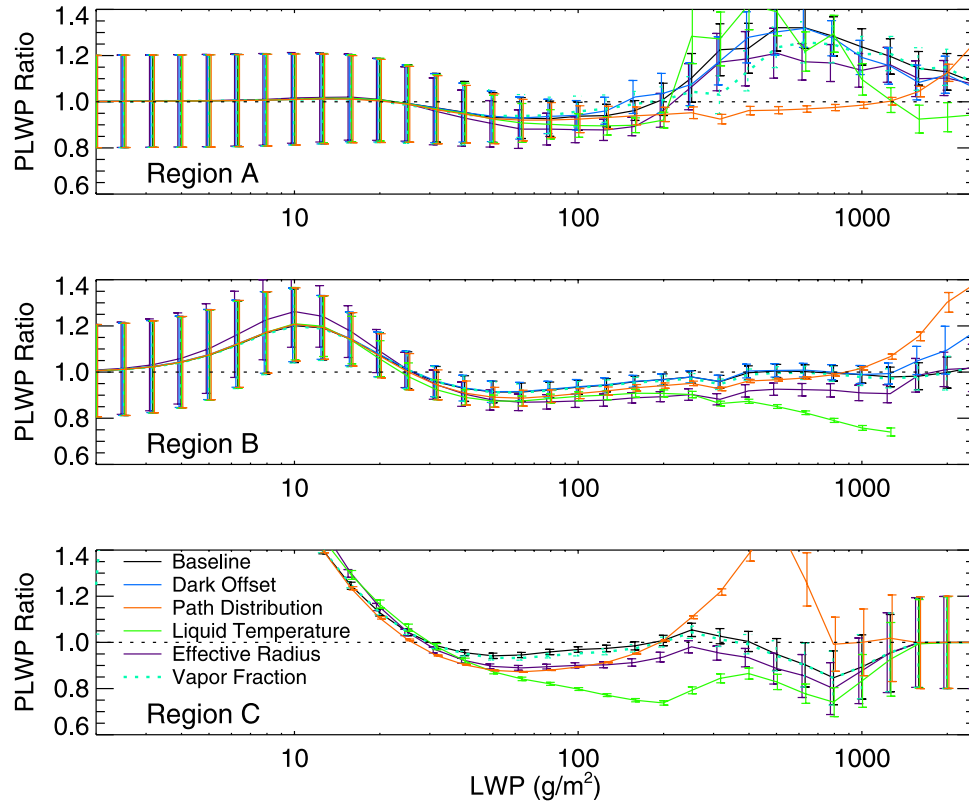


**Figure A1.** Ratios of retrieved PLWP to correct values demonstrating PLWP sensitivity to a changed fraction of vapor inside the cloud (35% versus 25%), a 10-count offset in the foreground spectrum, a changed cloud droplet effective radius ( $5\ \mu\text{m}$  versus  $10\ \mu\text{m}$ ), an  $\alpha$  fixed at 2.0, and the liquid cloud temperature fixed at 270 K for each of the three retrieval bands.

the retrieval seems to do a better job of reproducing the change of  $L^*$  with  $\tau'$  as calculated from diffusion theory.

## 5. Conclusions

[45] We have used calculations of zenith-sky spectral radiances to show the accuracy and precision with which several cloud quantities can be retrieved from ground-based observations using an optimal estimation differential optical absorption spectroscopy analytic technique. Known spectral features are fit to the ratio of a foreground to a background spectrum. The technique is relatively insensitive to slowly spectrally varying signals caused by processes such as Rayleigh and aerosol scattering. The three vapor, liquid, and ice absorption bands considered, between 0.9 and  $1.7\ \mu\text{m}$ , exhibit a large range in their absorption coefficients, which allows them to work in a complementary fashion to provide information about clouds ranging from the optically thin limit to clouds containing LWPs of greater than  $1000\ \text{g/m}^2$ . Cloud parameters that have been retrieved are path-integrated liquid water path (PLWP), path-integrated ice water path (PIWP), liquid and ice temperature, and a measure of the photon path distribution width. The cloud quantity estimates are sensitive to various assumptions in the retrieval technique with the sensitivities dependent on the cloud conditions. Thus care is required in determining which parameters should be retrieved and which should be fixed during any particular time period.

[46] We have analyzed data taken on 14 September 2004 in Barrow, Alaska, with this technique. Assuming plane-parallel conditions, we have calculated relationships between PLWP and LWP to compare our results to LWPs estimated from a collocated microwave radiometer. The agreement is encouraging, although the spectral retrievals tend to be lower than the LWP values estimated from the MWR. During periods of low LWPs, we have also compared our results to LWPs retrieved from a collocated atmospheric emitted radiance interferometer (AERI), demonstrating good agreement, and providing promise for the near-infrared technique to be useful in characterizing clouds of low LWP ( $10\text{--}50\ \text{g/m}^2$ ). Comparisons have also been made between retrieved PIWP and IWPs estimated from a collocated millimeter-wavelength cloud radar (MMCR). These estimates are highly correlated and demonstrate the potential of the near-infrared analysis method in mixed-phase conditions. Estimates also have been presented of cloud liquid temperature and a measure of the width of the photon path distribution and are compared to expected values. The photon path distribution width compares well with the diffusion limit calculations of *Davis and Marshak* [2002], and the cloud liquid temperature demonstrates agreement with the brightness temperatures retrieved by the AERI to within a few degrees for much of the measurement period. The results of these comparisons suggest that the spectral analysis technique can currently provide useful

**Table A1.** Cases Used to Examine the Sensitivity of PLWP Retrievals to Various Assumptions in the Retrieval Process<sup>a</sup>

Case	Details of Deviation From Baseline	Conditions When Most Significant for PLWP Estimate
A, baseline	-	-
B, dark offset	add 10 counts to foreground spectrum to simulate drift of zero level	relatively small (see section 3 for larger effect on $\alpha$ retrievals)
C, path distribution	assume $\alpha$ is fixed at 2.0 rather than being retrieved	when absorption no longer optically thin (large effect)
D, liquid temperature	fix liquid temperature at 270 K rather than the correct 260 K	moderate to large PLWP values (see Figure A1)
E, effective radius	fix radius at 5 $\mu\text{m}$ rather than the correct 10 $\mu\text{m}$	relatively small except when trying to correct PLWP values in optically thin limit
F, vapor fraction	assume 35% of vapor is in cloud rather than the 25% assumed in “baseline” case	relatively small

<sup>a</sup>PLWP, path-integrated liquid water path.

measurements of PLWP, PIWP, photon path distribution width and cloud liquid temperature.

## Appendix A

[47] A summary of the sensitivity of PLWP estimates to several analysis assumptions is presented in Figure A1 for retrievals using each of the three wavelength regions. The assumptions made in calculating the six cases considered are summarized in Table A1, as are the conditions under which each assumption is most important to the retrieval of PLWP. The baseline retrieval is shown in black in Figure A1. The deviation of the other curves relative to the baseline case is a measure of the retrieved PLWP sensitivity to these factors. The deviation of the baseline curve from 1 can be interpreted as largely due to errors in the retrieval approximation of the radiative transfer calculation.

[48] The sensitivities of the retrievals from the three spectral regions exhibit some important similarities. Perhaps most obvious is the importance of the path distribution parameter,  $\alpha$ , as  $\tau_{\text{abs}}$  gets large. However, it is also apparent that fixing the value of  $\alpha$  leads to reduced sensitivity to measurement noise, making this preferable to retrieving  $\alpha$  when  $\tau_{\text{abs}}$  is small enough that the retrieved value of the PLWP is not too affected by the choice of  $\alpha$ . The next most important PLWP sensitivity for Regions B and C is the choice of liquid temperature. Fixing the liquid temperature to an incorrect value leads to inferior PLWP estimates under moderate to thick clouds. Depending on the LWP range that is being retrieved, one would have to weigh the inaccuracy of fixing the liquid temperature at the a priori value against the potential errors induced by including liquid temperature in the retrieval process. The PLWP estimates demonstrate less sensitivity to the water vapor fraction assumed inside the cloud, a drift in the dark spectral offset, and to the spectral shape change induced by a different assumed  $r_{\text{eff}}$ . This minor importance of the spectral shape due to an  $r_{\text{eff}}$  assumption should not be confused with the substantial importance of  $r_{\text{eff}}$  in estimating the cloud path enhancement for optically thicker clouds and thus in relating PLWP to LWP, as is done in section 4.

[49] The effect of uncertainties in the water vapor profile on the retrieved PLWP is estimated by analyzing spectra generated for the dry vapor case with the wet water vapor profile and the wet vapor case with the dry profile, using a

constant background and a calculated background containing 43  $\text{g/m}^2$  LWP. Errors in the water vapor assumptions can certainly lead to significant retrieval errors, depending on what other quantities are retrieved in the analysis process and on how much vapor is in the atmosphere during the measurements. Indeed, we have already discussed the greater difficulties presented by a wetter atmospheric environment. However, from the cases discussed here, we find it much more important to have spectral background taken in a known atmospheric state than to be using the correct water vapor cross sections (when choosing between the two profiles considered here). In fact, if a cloudy-sky background is used, either of the vapor absorption coefficients (wet or dry) often allows for equally good PLWP retrievals. In contrast, if a spectrally constant background is used, there is a noticeable degradation in the PLWP accuracy when the incorrect vapor absorption coefficients are used.

## Appendix B

[50] In Figure 7, a comparison between the  $\alpha$  retrievals from calculated spectra and the direct values inferred from the multiple scattering model is performed. Unlike LWP,  $r_{\text{eff}}$ , and several other cloud properties, the value of  $\alpha$  is not a prescribed quantity in a radiative transfer (RT) model. So first, the “correct” value for the RT model must be determined. This is accomplished by starting with a nonabsorbing cloud of fixed LWP and then adding absorption in the form of reduced single scattering albedos (thus keeping the extinction optical depth fixed) in increments of  $4 \times 10^{-4}$ . For each of these varying coalbedos, the transmission ratio of the increased coalbedo case to the baseline case is related to the value of  $\alpha$  through the equivalence theorem

$$I = I_0 \int_0^{\infty} p(l) \exp(-l\gamma) dl, \quad (\text{B1})$$

substituting equation (6) as the path distribution form so

$$\frac{I}{I_0} = \alpha^\alpha (\alpha + l\gamma)^{-\alpha}, \quad (\text{B2})$$

where  $I_0$  is the downwelling intensity for the nonabsorbing cloud case and  $I$  is the same for the increased coalbedo case.

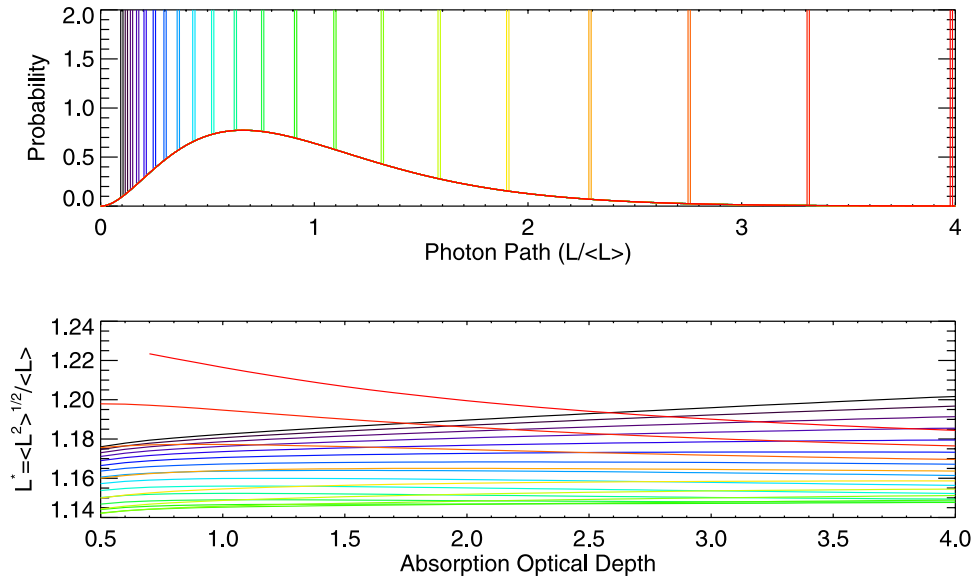


**Figure B1.** (top) Various photon path distributions. (bottom) Theoretically calculated variations of  $L^*$  with absorption optical depth for various photon path distributions of the top panel. The color codes in the bottom panel correspond to the distribution color codes in the top panel.

The value of  $l_y$  is the increase in the absorption optical depth across the cloud due to the coalbedo increase, multiplied by the cloud path enhancement. This then gives a unique calculation of  $\alpha$  for a range of coalbedos and LWPs.

[51] In some cases, it might be possible to probe further into the path distribution by exploiting the information available from the variation of  $\tilde{\omega}$ . As discussed in section 3, the value of  $L^*$  differs for various choices of  $\tilde{\omega}$ , and thus across the absorption spectrum, if the parameterization of the path distribution is imperfect. In the top panel of Figure B1, we show 21 path distribution functions of the form

$$p(\alpha, \langle l \rangle, l_0; l) = \frac{1}{\Gamma(\alpha)(\langle l \rangle / \alpha)^\alpha} l^{\alpha-1} \exp\left[-\frac{\alpha l}{\langle l \rangle}\right] + \varepsilon \delta(l_0), \quad (\text{B3})$$

where  $l_0$  is the location of a delta function path perturbation on the distribution of (6) that has an integrated area of  $\varepsilon$ ,  $\langle l \rangle$  is prescribed to be 1, and  $\alpha$  is assumed to be 3.0. The mean path length of the distribution is then

$$\langle l_{total} \rangle = \frac{1 + \varepsilon l_0}{1 + \varepsilon}. \quad (\text{B4})$$

The inferred values of  $L^*$  given this new mean path length, are shown in the bottom panel of Figure B1 as a function of both  $\tau_{abs}$  (x-axis) and path distribution (color). The  $\alpha$  values demonstrate variations in the previously discussed dependence on  $\tilde{\omega}$  and suggest the potential to use liquid absorption measurement at various wavelengths to estimate the way in which the actual path distribution might differ from equation (6).

## Appendix C

[52] There are additional points that must be considered in the application of equations (2)–(4) to measurements. First, account must be made for the potential shifting and

stretching of the diode/wavelength relationship due to changes in the spectrometer optics. This is addressed in the retrieval process by creating a new, changing diode/wavelength relationship as part of the analysis so that

$$i_{new} = i + shift + stretch \times \left( \frac{i - i_{mid}}{i_{total}} \right), \quad (\text{C1})$$

where  $i$  is the predefined pixel index that ranges from 0 to 255 and corresponds to known wavelengths, and shift and stretch are retrieved. The new pixel grid is then adjusted to this predefined pixel/wavelength relationship so the data and the cross sections are aligned in wavelength.

[53] It is important to obtain accurate shift and stretch values, as well as water vapor (and other gases), liquid, and ice abundances, applicable to the background spectrum. Errors in these values will propagate directly into errors in the foreground estimates. Even if water vapor estimates are not desired, for example, an inaccurate background value can lead to an inability to fit the differential vapor signal properly owing to nonlinearities in the convolved absorption cross section. This can then inhibit the accurate retrieval of liquid and ice. In general, it is desirable to choose a background spectrum that is characterized by similar amounts of interfering gases as the foreground spectra. This often leads to an improved ability to retrieve the quantities of interest. Furthermore, it is possible to approximate the atmospheric quantities of the background by retrieving them with this spectrum considered as the foreground spectrum in equation (2) and either a calibration lamp or a clear sky spectrum (if the column water vapor can be accurately estimated) as the background. In the analysis of measurements presented here, each analyzed spectrum is evaluated relative to an average of 10 cloudy-sky backgrounds taken at either 1024 ADT or 1311 ADT. The PLWPs (175 g/m<sup>2</sup> and 115 g/m<sup>2</sup>), the vapor amount, and the shift and stretch for these background spectra are

determined by analyzing them relative to the average of 10 clear sky spectra taken on 18 September, with the same values of that background determined relative to the spectrum of a halogen calibration lamp that is spectrally smooth relative to atmospheric measurements. A constant background is not used in the analysis of measurements, as was done with synthetic spectra, because the spectrum of the halogen lamp removes much of the effect of the low-frequency instrument response without the need to precisely know it.

[54] Another difference between analyzing data compared to calculated spectra concerns the potential drift in the dark background due to temperature variation at the detector, as well as the contribution of scattered light in the instrument. We have attempted to address this problem by placing a long-pass filter with a 50% transmission point at 1.0  $\mu\text{m}$  in front of the slit; this reduces the light at the shortest wavelengths to about 1% of its unfiltered intensity. It is then assumed that any deviation of the signal in this wavelength range is indicative of scattered light in the instrument or of dark drift. The average of the first 10 diodes ( $\sim 0.901\text{--}0.930\ \mu\text{m}$ ) is subtracted from each spectrum to correct for this effect. This correction procedure is imperfect, owing to the contribution, albeit small, of solar intensity passing through the filter at these shortest wavelengths and then being subtracted out incorrectly as a dark current drift. For the data presented in section 4, the magnitude of this signal identified as the dark current ranges from about  $-0.5\%$  to  $0.5\%$  ( $-30$  to  $+40$  counts) of the peak number of counts for each spectrum. Hence, in order to approximate an upper limit for the effect of an error in properly identifying the signal as a measure of the dark drift, the retrieval procedure is used to measure PLWP,  $\alpha$ , and liquid temperature during the period shown in Figures 10 and 13 after adding the same number of additional counts to every diode for each spectrum, calculated as 0.005 multiplied by the maximum counts registered by a particular diode for that spectrum. This leads to a small effect on the estimated PLWP ( $\pm 4\%$ ). The effect on retrieved temperature is more significant, with a reduction of 3–8 K throughout the period. The effect on the estimated value of  $\alpha$  is the most significant, as would be expected by the change in spectral shape, particularly near the centers of strong absorption features where the majority of the information concerning  $\alpha$  is found. The value of  $\alpha$  is reduced by an average of 0.5 throughout this time period compared to results of retrievals performed without the additional counts. While these effects are significant for both liquid temperature and  $\alpha$  estimates, we believe the errors after attempting to correct for the dark drift will be substantially less. Measurements on this day lead us to conclude that the first 10 diodes exhibit a response (in counts) of only about 0.1% of the peak counts in each spectrum. Hence the sensitivity study assuming 0.5% of the peak counts is likely to be dominated by true drifts in the dark current and should therefore be accounted for correctly.

[55] Finally, imperfect modeling of the instrument response to a given spectrum can introduce additional uncertainties to the retrieval process. A few examples of imperfections that can be important include the deviation from the assumed instrument slit function, a detector response that deviates from being linear with spectral

intensity, and spectral response stability. The stability of the spectral response over the measurements period is estimated from spectra taken periodically of a broadband calibration lamp. Six such spectra were taken between 16 and 21 September. The absolute intensity response varies by less than 3% among these observations, with the spectrally structured variations being much less. In fact, if successive lamp spectra are used as foreground and background spectra in equation (2), the effect of spectral variations leads to a maximum inferred PLWP value of less than  $2\ \text{g/m}^2$  and a maximum inferred PIWP of less than  $1\ \text{g/m}^2$ . These observations suggest that any variation in the spectral stability of the instrument should be of very minor importance to our retrievals.

[56] Laboratory studies have been performed to estimate the extent of the nonlinear response and the deviation of the slit function from a simple Gaussian shape. The nonlinearity, determined by measuring the output from a tungsten-halogen lamp at many different integration times maximizes at about 3% at 20,000 counts with little change for greater intensity. For reference, the maximum intensity measured on 14 September was about 45,000 counts, but the peak intensity of more than 95% of the spectra was under 20,000 counts. The slit function was estimated from observations of emission lines from a Hg/Ar lamp in the wavelength region 1.22  $\mu\text{m}$  to 1.35  $\mu\text{m}$ . While a Gaussian slit function with a FWHM of about 5.0 nm does a good job of fitting the lines out to roughly 10% of the peak intensity, the regions between the lines cannot be adequately described by a slit function that falls off this quickly in the wings. We find that a slit function described by

$$K(\lambda) = \exp\left\{-\left(\frac{\lambda - \lambda_0}{2.65}\right)^2\right\} + \frac{1}{15(|\lambda - \lambda_0| + 1)} \quad (\text{C2})$$

performs much better, where  $\lambda_0$  is the center wavelength. Analyses of the 14 September observations from 10:00 to 11:30 local time have been performed with this function, with a Gaussian function characterized by a FWHM of 4.41 nm, and with a Gaussian function with a FWHM of 5.00 nm (equivalent to 3.00 in the denominator of the first term of equation (C2) in place of the 2.65) to estimate the potential effect of errors in the slit function on the retrievals. Analyses using Region B/C show that the effect of not including the second term in equation (C2) is the most significant of these assumptions in the retrieval of  $\alpha$ , PLWP, and liquid temperature (ice was not retrieved). The maximum impact on the PLWP retrievals ranged from  $-5$  to  $25\ \text{g/m}^2$ , or about  $-6\%$  to  $8\%$  of the inferred PLWP with the rms over the period of  $6\ \text{g/m}^2$ . The maximum effect on temperature was  $-6\ \text{K}$  to  $8\ \text{K}$  with an rms of 3 K. The effect on  $\alpha$  is always less than  $\pm 0.4$  except for 2 of the 126 retrieved values during this period that exhibit differences of more than 0.8. The rms over this period is 0.2. These results suggest that an inaccurate estimate of the instrument slit function can lead to retrieval errors that can be of some importance when highly accurate estimates are desired. Compared to the slit function, the effects of the nonlinear detector response and the change of the FWHM from 4.41 nm to 5.00 nm are much smaller for each of these retrieved parameters.

[57] **Acknowledgments.** We thank the United States Department of Energy as part of the Atmospheric Radiation Measurement Program Climate Research Facility for allowing us to make our measurements at their Barrow, Alaska, facility, and for allowing us the use of coincident supportive data. We thank Walter Brower, Jimmy Ivanoff, and Gilbert Leavitt for their assistance in Barrow during this measurement period. We thank Ping Yang for sending us his ice particle scattering and absorption properties. We thank Anthony Davis for helpful discussions regarding the photon path distribution, and we thank two reviewers for their useful comments. R. S. would also like to thank the CIRES Visiting Fellowship Program for providing funding.

## References

- Ackerman, S. A., W. L. Smith, J. D. Spinhirne, and H. E. Revercomb (1990), The 27–28 October 1986 FIRE IFO cirrus case study: Spectral properties of cirrus clouds in the 8–12  $\mu\text{m}$  window, *Mon. Weather Rev.*, *118*, 2377–2388.
- Ackerman, S. A., W. L. Smith, A. D. Collard, X. L. Ma, H. E. Revercomb, and R. O. Knuteson (1995), Cirrus cloud properties derived from high spectral resolution infrared spectrometry during FIRE II, part II, Aircraft HIS results, *J. Atmos. Sci.*, *52*(23), 4246–4263.
- Arking, A., and J. D. Childs (1985), Retrieval of cloud cover parameters from multispectral satellite images, *J. Clim. Appl. Meteorol.*, *24*, 322–333.
- Baum, B. A., P. F. Soulen, K. I. Strabala, M. D. King, S. A. Ackerman, W. P. Menzel, and P. Yang (2000), Remote sensing of cloud properties using MODIS airborne simulator imagery during SUCCESS, 2, Cloud thermodynamic phase, *J. Geophys. Res.*, *105*(D9), 11,781–11,792.
- Betts, A. K., and Harshvardhan (1987), Thermodynamic constraint on the cloud liquid water feedback in climate models, *J. Geophys. Res.*, *92*, 8483–8485.
- Clough, S. A., M. W. Shephard, E. J. Mlawer, J. S. Delamere, M. J. Iacono, K. Cady-Pereira, S. Boukabara, and R. D. Brown (2005), Atmospheric radiative transfer modelling: A summary of the AER codes, *J. Quant. Spectrosc. Radiat. Transfer*, *91*, 233–244.
- Crewell, S., and U. Löhnert (2003), Accuracy of cloud liquid water path from ground-based microwave radiometry: 2. Sensor accuracy and synergy, *Radio Sci.*, *38*(3), 8042, doi:10.1029/2002RS002634.
- Daniel, J. S., S. Solomon, R. W. Sanders, R. W. Portmann, D. C. Miller, and W. Madsen (1999), Implications for water monomer and dimer solar absorption from observations at Boulder, Colorado, *J. Geophys. Res.*, *104*, 16,785–16,791.
- Daniel, J. S., S. Solomon, R. W. Portmann, A. O. Langford, C. S. Eubank, E. G. Dutton, and W. Madsen (2002), Cloud liquid water and ice measurements from spectrally resolved near-infrared observations: A new technique, *J. Geophys. Res.*, *107*(D21), 4599, doi:10.1029/2001JD000688.
- Davis, A. B., and A. Marshak (2002), Space-time characteristics of light transmitted through dense clouds: A Green's function analysis, *J. Atmos. Sci.*, *59*, 2713–2727.
- Deeter, M. N., and K. F. Evans (2000), A novel ice-cloud retrieval algorithm based on the Millimeter-Wave Imaging Radiometer (MIR) 150- and 220-GHz channels, *J. Appl. Meteorol.*, *39*, 623–633.
- Del Genio, A. D., and A. B. Wolf (2000), The temperature dependence of the liquid water path of low clouds in the southern Great Plains, *J. Clim.*, *13*, 3465–3486.
- Evans, K. F., S. J. Walter, A. J. Heymsfield, and M. N. Deeter (1998), Modeling of submillimeter passive remote sensing of cirrus clouds, *J. Appl. Meteorol.*, *37*, 184–205.
- Evans, K. F., A. H. Evans, I. G. Nolt, and B. T. Marshall (1999), The prospect for remote sensing of cirrus clouds with a submillimeter-wave spectrometer, *J. Appl. Meteorol.*, *38*, 514–525.
- Flynn, C. (2004), Micropulse lidar (MPL) handbook, *ARM TR-019*, 10 pp., U. S. Dept. of Energy, Washington, D. C.
- Frisch, A. S., C. W. Fairall, and J. B. Snider (1995), Measurement of stratus cloud and drizzle parameters in ASTEX with a  $K_{\alpha}$ -band Doppler radar and a microwave radiometer, *J. Atmos. Sci.*, *52*(16), 2788–2799.
- Grundy, W. M., and B. Schmitt (1998), The temperature-dependent near-infrared absorption spectrum of hexagonal  $\text{H}_2\text{O}$  ice, *J. Geophys. Res.*, *103*, 25,809–25,822.
- Han, Q., W. Rossow, R. Welch, A. White, and J. Chou (1995), Validation of satellite retrievals of cloud microphysics and liquid water path using observations from FIRE, *J. Atmos. Sci.*, *52*(23), 4183–4195.
- Hansen, J. E., and J. B. Pollack (1970), Near-infrared light scattering by terrestrial clouds, *J. Atmos. Sci.*, *27*, 265–281.
- Heney, L. C., and J. L. Greenstein (1941), Diffuse radiation in the galaxy, *Astrophys. J.*, *93*, 70–83.
- Heymsfield, A., S. Matrosov, and B. Baum (2000), Ice water path-optical depth relationships for cirrus and deep stratiform ice cloud layers, *J. Appl. Meteorol.*, *42*, 1369–1390.
- Hinkley, E. D. (1976), *Laser Monitoring of the Atmosphere, Topics Appl. Phys.*, vol. 14, Springer, New York.
- Intergovernmental Panel on Climate Change (IPCC) (2001), *Climate Change 2001: The Scientific Basis*, Cambridge Univ. Press, New York.
- Johnson, D. W., et al. (2000), An overview of the Lagrangian experiment undertaken during the North Atlantic regional Aerosol Characterisation Experiment (ACE-2), *Tellus, Ser. B*, *52B*, 290–320.
- Jursa, A. S. (1985), *Handbook of Geophysics and the Space Environment*, Air Force Geophys. Lab., Hanscom Air Force Base, Mass.
- Kawamoto, K., T. Y. Nakajima, and N. Nakajima (2001), A global determination of cloud microphysics with AVHRR remote sensing, *J. Clim.*, *14*, 2054–2068.
- King, M. D., S.-C. Tsay, S. Platnick, M. Wang, and K.-N. Kiou (1997), Cloud retrieval algorithms for MODIS: Optical thickness, effective particle radius, and thermodynamic phase, *Rep. ATBD-MOD-05*, 83 pp., NASA Goddard Space Flight Cent., Greenbelt, Md.
- Kou, L., D. Labrie, and P. Chylek (1993), Refractive indices of water and ice in the 0.65- to 2.5- $\mu\text{m}$  spectral range, *Appl. Opt.*, *32*, 3531–3540.
- Langford, A. O., R. W. Portmann, J. S. Daniel, H. L. Miller, C. S. Eubank, S. Solomon, and E. G. Dutton (2005), Retrieval of ice crystal effective diameters from ground-based near-infrared spectra of optically thin cirrus, *J. Geophys. Res.*, *110*, D22201, doi:10.1029/2005JD005761.
- Lin, B., B. Wielicki, P. Minnis, and W. Rossow (1998), Estimation of water cloud properties from satellite microwave, infrared and visible measurements in oceanic environments, 1, Microwave brightness temperature simulations, *J. Geophys. Res.*, *103*(D4), 3873–3886.
- Lin, B., P. Minnis, and A. Fan (2003), Cloud liquid water path variations with temperature observed during the Surface Heat Budget of the Arctic Ocean (SHEBA) experiment, *J. Geophys. Res.*, *108*(D14), 4427, doi:10.1029/2002JD002851.
- Liou, K. N., S. C. Ou, Y. Takano, F. P. J. Valero, and T. P. Ackerman (1990), Remote sounding of the tropical cirrus cloud temperature and optical depth using 6.5 and 10.5  $\mu\text{m}$  radiometers during STEP, *J. Appl. Meteorol.*, *29*, 716–726.
- Liu, C.-L., and A. J. Illingworth (2000), Toward more accurate retrievals of ice water content from radar measurements of clouds, *J. Appl. Meteorol.*, *39*, 1130–1146.
- Liu, G., and J. A. Curry (1998), Remote sensing of ice water characteristics in tropical clouds using aircraft microwave measurements, *J. Appl. Meteorol.*, *37*, 337–355.
- Lohmann, U., and J. Feichter (2005), Global indirect aerosol effects: A review, *Atmos. Chem. Phys.*, *5*, 715–737.
- Löhnert, U., and S. Crewell (2003), Accuracy of cloud liquid water path from ground-based microwave radiometry, 1, Dependency on cloud model statistics, *Radio Sci.*, *38*(3), 8041, doi:10.1029/2002RS002654.
- Marshak, A., A. Davis, W. Wiscombe, and R. Cahalan (1995), Radiative smoothing in fractal clouds, *J. Geophys. Res.*, *100*, 26,247–26,261.
- Matrosov, S. Y., T. Uttal, J. B. Snider, and R. A. Kropfli (1992), Estimations of ice cloud parameters from ground-based infrared radiometer and radar measurements, *J. Geophys. Res.*, *97*(D11), 11,567–11,574.
- Matrosov, S. Y., B. W. Orr, R. A. Kropfli, and J. B. Snider (1994), Retrievals of vertical profiles of cirrus cloud microphysical parameters from Doppler radar and infrared radiometer measurements, *J. Appl. Meteorol.*, *33*, 617–626.
- Miller, S. D., G. L. Stephens, C. K. Drummond, A. K. Heidinger, and P. T. Partain (2000), A multisensor diagnostic satellite cloud property retrieval scheme, *J. Geophys. Res.*, *105*(D15), 19,955–19,971.
- Min, Q., and E. E. Clothiaux (2003), Photon path length distributions inferred from rotating shadowband spectrometer measurements at the Atmospheric Radiation Measurements Program Southern Great Plains site, *J. Geophys. Res.*, *108*(D15), 4465, doi:10.1029/2002JD002963.
- Min, Q., and L. C. Harrison (1996), Cloud properties derived from surface MFRSR measurements and comparison with GOES results at the ARM SGP site, *Geophys. Res. Lett.*, *23*(13), 1641–1644.
- Min, Q.-L., and L. C. Harrison (1999), Joint statistics of photon path length and cloud optical depth, *J. Geophys. Res.*, *26*, 1425–1428.
- Min, Q.-L., L. C. Harrison, and E. E. Clothiaux (2001), Joint statistics of photon path length and cloud optical depth: Case studies, *J. Geophys. Res.*, *106*, 7375–7386.
- Min, Q.-L., M. Duan, and R. Marchand (2003), Validation of surface retrieved cloud optical properties with in situ measurements at the Atmospheric Radiation Measurement Program (ARM) South Great Plains site, *J. Geophys. Res.*, *108*(D17), 4547, doi:10.1029/2003JD003385.
- Min, Q.-L., L. C. Harrison, P. Kiedron, J. Berndt, and E. Joseph (2004), A high-resolution oxygen A-band and water vapor band spectrometer, *J. Geophys. Res.*, *109*, D02202, doi:10.1029/2003JD003540.
- Minnis, P., K.-N. Liou, and Y. Takano (1993), Infrared radiances, part I, Parameterization of radiance fields, *J. Atmos. Sci.*, *50*(9), 1279–1304.

- Moran, K. P., B. E. Martner, M. J. Post, R. A. Kropfli, D. C. Welsh, and K. B. Widener (1998), An unattended cloud-profiling radar for use in climate research, *Bull. Am. Meteorol. Soc.*, **79**, 443–455.
- Morris, V. R. (2005), Microwave radiometer handbook, 22 pp., U. S. Dept. of Energy, *Tech. Rep. ARM TR-016*, Washington, D. C.
- Nakajima, T., and M. D. King (1990), Determination of the optical thickness and effective particle radius of clouds from reflected solar radiation measurements, part I, Theory, *J. Atmos. Sci.*, **47**(15), 1878–1893.
- Nakajima, T. Y., and N. Nakajima (1995), Wide-area determination of cloud microphysical properties from NOAA AVHRR measurements for FIRE and ASTEX regions, *J. Atmos. Sci.*, **52**(23), 4043–4059.
- Nakajima, T., and M. Tanaka (1988), Algorithms for radiative intensity calculations in moderately thick atmospheres using a truncation approximation, *J. Quant. Spectrosc. Radiat. Transfer*, **40**, 51–69.
- Ou, S. C., K. N. Liou, W. M. Gooch, and Y. Takano (1993), Remote sensing of cirrus cloud parameters using advanced very-high-resolution radiometer 3.7- and 10.9- $\mu\text{m}$  channels, *Appl. Opt.*, **32**(12), 2171–2180.
- Pfeilsticker, K., F. Erle, O. Funk, H. Veitel, and U. Platt (1998), First geometrical path lengths probability density function derivation of the skylight from spectroscopically highly resolving oxygen A-band observations, 1, Measurement technique, atmospheric observations and model calculations, *J. Geophys. Res.*, **103**, 11,483–11,504.
- Pilewskie, P., and S. Twomey (1987), Discrimination of ice from water in clouds by optical remote sensing, *Atmos. Res.*, **21**, 113–122.
- Platnick, S. (2000), Vertical photon transport in cloud remote sensing problems, *J. Geophys. Res.*, **105**, 22,919–22,935.
- Platt, C. M. R. (1973), Lidar and radiometric observations of cirrus clouds, *J. Atmos. Sci.*, **30**, 1191–1204.
- Ramanathan, V., E. J. Pitcher, R. C. Malone, and M. L. Blackmon (1983), The response of a spectral general circulation model to refinements in radiative processes, *J. Atmos. Sci.*, **40**, 605–630.
- Rodgers, C. D. (2000), *Inverse Methods for Atmospheric Sounding: Theory and Practice*, 238 pp., World Sci., London.
- Rothman, L. S., C. P. Rinsland, A. Goldman, and S. T. Massie (1998), The HITRAN molecular spectroscopic database and HAWKS (HITRAN Atmospheric WorkStation): 1996 edition, *J. Quant. Spectrosc. Radiat. Transfer*, **60**, 665–710.
- Sagan, C., and J. B. Pollack (1967), Anisotropic nonconservative scattering and the clouds of Venus, *J. Geophys. Res.*, **72**(2), 469–477.
- Segelstein, D. (1981), *The Complex Refractive Index of Water*, Univ. of Missouri, Kansas City.
- Shupe, M. D., and J. M. Intrieri (2004), Cloud radiative forcing of the Arctic surface: The influence of cloud properties, surface albedo, and solar zenith angle, *J. Clim.*, **17**(3), 616–628.
- Shupe, M. D., T. Uttal, S. Y. Matrosov, and A. S. Frisch (2001), Cloud Water Contents and Hydrometeor Sizes During the FIRE Arctic Clouds Experiment, *J. Geophys. Res.*, **106**(D14), 15,015–15,028.
- Shupe, M. D., T. Uttal, and S. Y. Matrosov (2005), Arctic cloud microphysics retrievals from surface-based remote sensors at SHEBA, *J. Appl. Meteorol.*, **44**, 1544–1562.
- Somerville, R. J. C., and L. A. Remer (1984), Cloud optical thickness feedbacks in the CO<sub>2</sub> climate problem, *J. Geophys. Res.*, **89**, 9668–9672.
- Stamnes, K., S. C. Tsay, W. Wiscombe, and K. Jayaweera (1988), A numerically stable algorithm for discrete-ordinate-method radiative transfer in scattering and emitting layered media, *Appl. Opt.*, **27**, 2502–2509.
- Strabala, K. I., S. A. Ackerman, and W. P. Menzel (1994), Cloud properties inferred from 8–12- $\mu\text{m}$  data, *J. Appl. Meteorol.*, **33**, 212–229.
- Sun, Z., and L. Rikus (1999), Parameterization of effective sizes of cirrus cloud particles and its verification against observations, *Q. J. R. Meteorol. Soc., Part B*, **12**(560), 3037–3055.
- Szejwach, G. (1982), Determination of semi-transparent cirrus cloud temperature from infrared radiances: Application to METEOSAT, *J. Appl. Meteorol.*, **21**, 384–393.
- Turner, D. D. (2005), Arctic mixed-phase cloud properties from AERI-lidar observations: Algorithm and results from SHEBA, *J. Appl. Meteorol.*, **44**, 427–444.
- Turner, D. D., S. A. Ackerman, B. A. Baum, H. E. Revercomb, and P. Yang (2003), Cloud phase determination using ground-based AERI observations at SHEBA, *J. Appl. Meteorol.*, **42**, 701–715.
- Turner, D. D., R. O. Knuteson, H. E. Revercomb, C. Lo, and R. G. Dedecker (2006), Noise reduction of Atmospheric Emitted Radiance Interferometer (AERI) observations using principal component analysis, *J. Atmos. Oceanic Technol.*, in press.
- Twomey, S., and T. Cocks (1989), Remote sensing of cloud parameters from spectral reflectance in the near-infrared, *Contrib. Atmos. Phys.*, **62**(3), 172–179.
- Van de Hulst, H. C. (1980), *Multiple Light Scattering: Tables, Formulas, and Applications*, 739 pp., Elsevier, New York.
- Veitel, H., O. Funk, C. Kruz, U. Platt, and K. Pfeilsticker (1998), Geometrical path length probability density functions of the skylight transmitted by mid-latitude cloud skies: Some case studies, *Geophys. Res. Lett.*, **25**, 3355–3358.
- Wendisch, M., P. Pilewskie, E. Jakel, S. Schmidt, J. Pommier, S. Howard, H. H. Jonsson, H. Guan, M. Schroder, and B. Mayer (2004), Airborne measurements of areal spectral surface albedo over different sea and land surfaces, *J. Geophys. Res.*, **109**, D08203, doi:10.1029/2003JD004392.
- Westwater, E. (1978), The accuracy of water vapor and cloud liquid determination by dual-frequency ground-based microwave radiometry, *Radio Sci.*, **13**, 677–685.
- Wilczak, J. M., E. E. Gossard, W. D. Neff, and W. L. Eberhard (1996), Ground-based remote sensing of the atmospheric boundary layer: 25 years of progress, *Boundary Layer Meteorol.*, **78**, 321–349.
- Wiscombe, W. J. (1979), Mie scattering calculations: Advances in technique and fast, vector-speed computer codes, *Rep. TN-140+STR*, Natl. Cent. for Atmos. Res., Boulder, Colo.
- Yang, P., K. N. Liou, K. Wyser, and D. Mitchell (2000), Parameterization of the scattering and absorption properties of individual ice crystals, *J. Geophys. Res.*, **105**(D4), 4699–4718.
- Zhao, L., and F. Weng (2002), Retrieval of ice cloud parameters using the advanced microwave sounding unit, *J. Appl. Meteorol.*, **41**, 384–395.

---

J. S. Daniel, C. S. Eubank, A. O. Langford, H. L. Miller, R. W. Portmann, R. Schofield, and S. Solomon, Aeronomy Laboratory, NOAA, 325 Broadway, Boulder, CO 80305, USA. (john.s.daniel@noaa.gov)  
 M. D. Shupe, Cooperative Institute for Research in Environmental Sciences, University of Colorado, Boulder, CO 80309, USA.  
 D. D. Turner, University of Wisconsin, Madison, WI 53706, USA.